Rim-Mounted Reconfigurable Surfaces for Interference Nulling in Focus-Fed Axisymmetric Reflector Antenna Systems

Alec Johnathan Yip

Thesis submitted to the faculty of the
Virginia Polytechnic Institute and State University
in partial fulfillment of the
requirements for the degree of

Master of Science
In
Electrical Engineering

Steven Ellingson, Chair
Richard Buehrer
Bradley Davis

August 9, 2024
Blacksburg, Virginia

Keywords: Adaptive antennas

Rim-Mounted Reconfigurable Surfaces for Interference Nulling in Focus-Fed Axisymmetric Reflector Antenna Systems

Alec Johnathan Yip

ACADEMIC ABSTRACT

This thesis addresses the use of an electronic reconfigurable surface (ERS) attached to an axisymmetric paraboloidal reflector antenna to mitigate interference through nulling for radio astronomy applications. The ERS is a reflectarray that consists of multiple elements, which can be electronically controlled to modify the reflected field. Previous research focused on a "conformal" system with elements placed on a paraboloidal surface extending beyond the unmodified reflector. These studies concluded that nulling could be achieved without compromising the gain and shape of the main lobe. This thesis builds on previous research by addressing two topics. The first topic is minimization of the ERS rim width. A closed form expression for the minimum width required for effective nulling in the close-in sidelobes is derived in this thesis. The second topic addressed in this thesis is ERS configurations comprised of flat panels as an alternative to the conformal ERS implementation. Flat panels may be easier to manufacture compared to their conformal counterpart. Flat panel ERS implementations are evaluated, and it is concluded that they are a suitable alternative to conformal ERS implementation.

Rim-Mounted Reconfigurable Surfaces for Interference Nulling in Focus-Fed Axisymmetric Reflector Antenna Systems

Alec Johnathan Yip

GENERAL AUDIENCE ABSTRACT

This thesis utilizes the state-of-the art electronic reconfigurable surface (ERS) attached to a reflector antenna to mitigate interference for radio astronomy applications. The ERS is an array that can be controlled electronically to modify the radiation from the reflector. Previous research focused on configuring the ERS attached conformally to the reflector to null interference in a direction. This thesis appends previous research by addressing two topics. The first topic is the minimization of the ERS width for the conformal implementation. A closed form expression for the minimum ERS width is derived in this thesis. The second topic is to explore an ERS topology that consists of flat panels attached to the reflector. This topology is explored since flat ERS panels may be easier to manufacture. It is concluded that the flat panel ERS implementation is a suitable alternative to the conformal ERS implementation for interference mitigation.

Acknowledgements

This work was supported in part by National Science Foundation Grants ECCS-2029948 and AST-2128506.

First and foremost, I would like to thank my thesis advisor, Dr. Steven W. Ellingson, for his invaluable time, knowledge, and patience with me and my master's thesis. Additionally, I would also like to offer my gratitude and thanks to Dr. R. Michael Buehrer and Dr. Bradley Davis for serving on my thesis committee.

I would also like to express my gratitude to my friend, Joseph Vance Rielly for being a great friend throughout the years.

I would also like to express my thanks and love to my family (Kwan Chan, Robert Yip, and Gordon Yip) for supporting me immensely through my education.

Lastly, I would like to express my thanks and love to Olivia Moldoveanu who, along with my father, painstakingly edited my thesis.

Blacksburg, Virginia — Alec J. Yip
August 9, 2024

Table of Contents

List of Figures

List of Tables

Chapter 1

Introduction

Radio astronomy is the study of astronomical phenomena using electromagnetic signals in the radio or microwave frequency bands [1]. A suitable candidate for capturing these signals is the focus-fed axisymmetric paraboloidal reflector antenna [2]. An example of the aforementioned antenna is shown in Figure 1.1. These antennas are used for their high gain, which leads to a high spatial selectivity. Although there is feed blockage and scattering from the feed support structures, the cost and ease of design compared to other antennas makes it a popular choice.

It should be noted that maximum gain is not the only requirement for radio astronomers. In fact, many radio astronomers focus on the polarization of the electromagnetic waves emanating from these astronomical phenomena, including pulsars [4]. This leads many radio astronomers to focus on methods to obtain polarization purity. Additionally, many radio astronomers face the issue of gain instability. For example, gain instability may be introduced in post-detection, which may cause issues when interpreting data. Thus, it is of interest to many radio astronomers to limit the gain variation.

An issue plaguing radio astronomy is interference from man-made transmissions; e.g., low earth orbit satellites [5], making interference mitigation increasingly necessary. One approach to interference mitigation is creating a null in the pattern (nulling) in the direction of the interference. A method to create a null is to use a phased array feed for the reflector system; see e.g., [6]. However, this usually leads to dynamic variability in the gain and shape of the main lobe.

Recently, another method for nulling has been proposed: The electronically reconfigurable surface (ERS) [7]. See Figure 1.2 for an example of a conformal ERS attached to the rim of an axisymmetric paraboloidal reflector. An ERS is a reflectarray which can electronically control the reflection from its elements. In [7], the ERS was modeled as a surface of perfectly electrical conducting $\lambda/2 \times \lambda/2$ square plates extending past the original reflector; i.e., "rim-mounted" and "conformal" (to the defining paraboloid), and was analyzed using physical optics. The results demonstrated that nulling in the close-in sidelobes could be achieved.

However, there were three concerns not addressed in [7]. The first concern was the validity of the approximate physical optics results compared to a full-wave analysis using practical phase-shifting elements. To address this, the authors of [9] conducted a full-wave analysis of

Figure 1.1: The Green Bank 20-Meter Telescope, an example of a focus-fed axisymmetric paraboloidal reflector antenna. Picture is sourced from [3].

a reflector system with an ERS comprised of practical components and compared the results to [7]. The study showed reasonable agreement with the physical optics model within the first few sidelobes.

The second concern was the issue of the dynamic variability of the main lobe gain and shape caused by the ERS as the null tracks the moving interferer. In response to this, [10] and [11] described and demonstrated effective algorithms for ERS nulling while constraining the main lobe.

The third concern was about the feasibility of a practical ERS implementation, where losses and electromagnetic coupling are issues. The authors of [12] analyzed the reflector system while modeling the ERS elements as patch antennas with pin diodes for phase control. This study concluded that nulling of the close-in sidelobes could be achieved with negligible loss of radiation efficiency.

Before considering testing of the ERS concept in physical hardware, there are two issues remaining. The first is determining the minimum useful width of the ERS rim. Minimizing the width of the ERS would reduce the cost and weight of the system. The second issue is to consider ERS implementations using flat panels, as shown in Figure 1.3. Approximating a conformal implementation using flat panels will be an attractive alternative due to manufacturing simplicity.

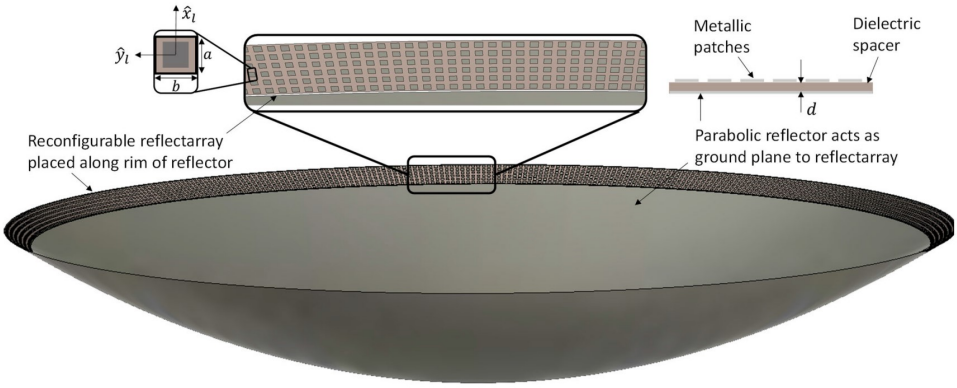

Figure 1.2: Conformal ERS attached to the rim of an axisymmetric paraboloidal reflector (Image Credit: [8]).

1.1 Problem Statement

Addressing the issues identified in the previous section, this thesis will:

- Derive an approximate closed-form expression for the minimum width of a rim-mounted ERS required to create a theoretically perfect null anywhere within a specified number of close-in sidelobes.
- Analyze ERS implementations that consist of flat rectangular panels – i.e., "outrigger panels"– that extend from the rim of the traditional non-reconfigurable portion of the reflector.

1.2 Contributions of this Thesis

The contributions of this thesis are as follows:

- Developed an approximate, closed-form expression for the minimum width required to create a theoretically perfect null anywhere within a specified number of close-in sidelobes. This is derived in Section 4.5 and the final result is Equation 4.30. Through an example in the same section, it is shown that the minimum rim width calculated using Equation 4.30 is in agreement with the result generated using physical optics assuming continuous phase variation of the ERS states. A limitation is that Equation 4.30 underestimates the size of the conformal ERS rim for discrete phase control of the ERS (i.e., 1-bit, 2-bit, etc.).
- Analyzed four outrigger panel configurations (Cases A, B, C, and D, as defined in Table 5.1) when the ERS is in the quiescent, maximum (i.e., set to maximize gain),

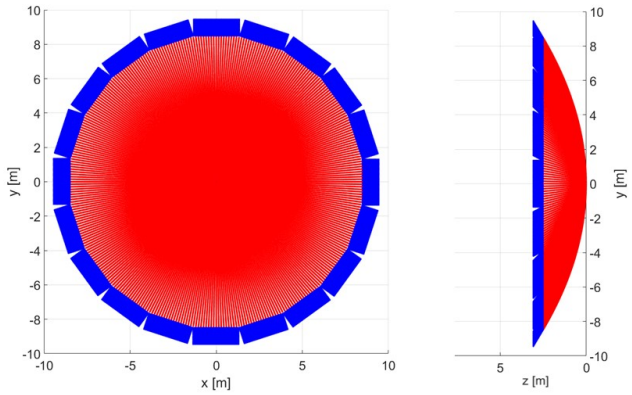

Figure 1.3: Outrigger panel system with 20 panels (blue) attached tangent to the rim of the non-reconfigurable reflector (red). Note that each outrigger panel consists of many ERS elements. The design parameters for this particular system are given by Case A in Table 5.2.

and nulling states. The analyses are presented in Sections 5.3-5.6, and the results are summarized in Section 5.7, specifically in Table 5.8. While all four outrigger panel configurations achieved nulling in the desired direction, the configurations exhibited different tradeoffs with respect to gain and cross-pol.

Note that the designs considered thus far are only at a single frequency. Assuming that the reflectarray consists of patch-like antennas, the frequency response is generally narrowband [13]. Additionally, the algorithms used to set the state vectors of the ERS for nulling do not consider bandwidth (see Section 2.3). Therefore, the designs are purely single-band.[1]

1.3 Organization of this Thesis

The remainder of this thesis is structured as follows:

Chapter 2, **Theory**, defines both the system geometry and the method of physical optics that is used to calculate the radiation patterns. This chapter concludes with an explanation of the feed model used throughout this thesis.

Chapter 3, **Implementation of the Physical Optics Model**, describes the implementation of the theory from Chapter 2 to calculate the pattern of the reflector system. The chapter concludes with the evaluation of two systems: One with no ERS, and one with a conformal ERS implementation, as in [7]. The former serves as a baseline for comparison

[1]Future work could focus on making these designs multi-band.

for the examples in Chapter 4, while the latter serves as a baseline for comparison for the examples of the non-conformal ERS implementations of Chapter 5.

Chapter 4, **Determining the Width of the ERS Rim**, first derives an approximate, closed-form expression for the scattered electric field from a reflector with a conformal ERS implementation. Using this expression, a closed-form expression for the minimum rim width of the ERS rim to null the m^{th} sidelobe is derived (see Equation 4.30). The chapter concludes with an example validating the results calculated using Equation 4.30.

Chapter 5, **Outrigger Panel Concept**, details the design of four outrigger panel configurations. These configurations are analyzed and compared to the conformal ERS implementation. This chapter concludes with a comparison and assessment of the outrigger panel configurations.

Chapter 6, **Conclusions**, outlines the principal findings of this thesis and proposes future research germane to this topic.

Appendix A, **ERS Panel Geometry**, contains a derivation for the length of an outrigger panel, which is required in Section 5.1.

Appendix B, **ERS Panel Orientation**, contains a derivation for the orientation of an outrigger panel, which is required in Section 5.1.

Chapter 2

Theory

This chapter summarizes the geometry of a focus-fed, axisymmetric paraboloidal reflector antenna, the reconfigurable elements, the method used to calculate the scattered electric field, and the feed model. Throughout this thesis, the term "reflector" is used in lieu of "focus-fed, axisymmetric paraboloidal reflector", as this is the only antenna configuration considered.

The organization of this chapter is as follows: The geometry of the reflector is discussed in Section 2.1. Physical optics (PO), the method used to determine the equivalent surface current densities on the reflector's surface, is described in Section 2.2. The process to set the state of the reconfigurable elements is described in Section 2.3. Quantities used to quantify reflector system performance are defined in Section 2.4. Lastly, the polarization patterns and feed model are discussed in Sections 2.5 and 2.6, respectively.

2.1 Paraboloidal Reflector Geometry

In this thesis, two coordinate systems are defined: feed and global. These are depicted in Figure 2.1. The feed coordinate system is denoted with a subscript f, while the global coordinate system has no subscript. The origin of the global coordinate system, O, is at the vertex of the reflector, while the origin of the feed coordinate system, O_f, and feed phase center are at the focus of the reflector. The relationship between the basis vectors of the global and feed coordinate systems is:

$$\begin{aligned} \hat{\mathbf{x}} &= \hat{\mathbf{x}}_f \\ \hat{\mathbf{y}} &= -\hat{\mathbf{y}}_f \\ \hat{\mathbf{z}} &= -\hat{\mathbf{z}}_f \end{aligned} \tag{2.1}$$

In the global coordinate system, the paraboloid is defined by the following equation:

$$\rho^2 = 4fz \tag{2.2}$$

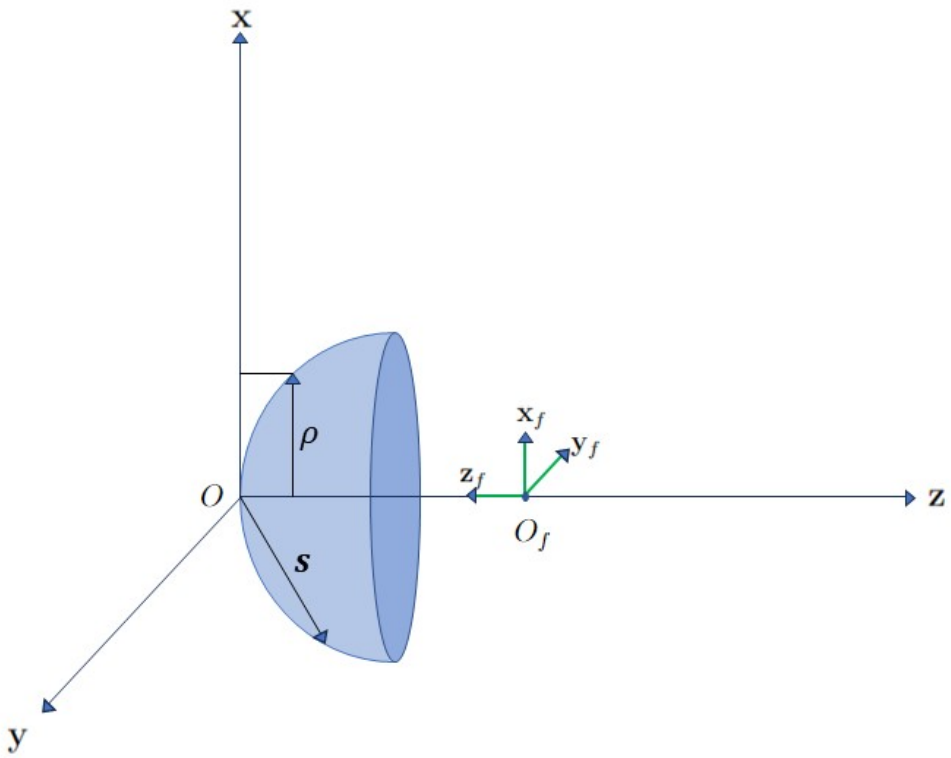

Figure 2.1: Reflector system in the feed and global coordinate systems.

where f is the focal length of the paraboloid, z is distance along the $+\hat{\mathbf{z}}$-axis, and ρ is the perpendicular displacement from the $\hat{\mathbf{z}}$-axis. Note that the focal length is the distance from the vertex of the reflector where the geometrical optics rays converge.

2.2 Field Computation using Physical Optics

PO is used as an alternative to solving Maxwell's equations for the field scattered from the reflector surface. Before proceeding, several simplifying assumptions are made regarding the reflector system:

- The wave impedance is the free space value, $\eta = \eta_0 \cong 377\ \Omega$.
- The reflector surface is a smooth, electrically large, perfect electrical conductor.
- Edge diffraction effects are ignored. These effects can be neglected since we will restrict our attention to main lobe and first two sidelobes [13].
- Feed antenna blockage can be ignored if the feed is small relative to the reflector.

The total scattered electric field intensity, $\mathbf{E}^s(\mathbf{r})$, from the reflector system is the sum of the electric field intensities from the non-reconfigurable and reconfigurable portions of the reflector ($\mathbf{E}_0^s(\mathbf{r})$ and $\mathbf{E}_r^s(\mathbf{r})$, respectively):

$$\mathbf{E}^s(\mathbf{r}) = \mathbf{E}_0^s(\mathbf{r}) + \mathbf{E}_r^s(\mathbf{r}) \tag{2.3}$$

These terms are considered in Sections 2.2.1 and 2.2.2, respectively.

2.2.1 Non-Reconfigurable Portion of the Reflector Surface

Let $\mathbf{E}^i$ be the electric field intensity radiated from the feed. Note that $\mathbf{s}_f$ is the vector from O_f to a point on the reflector, as shown in Figure 2.2. The equivalent surface current density at $\mathbf{s}_f$, $\mathbf{J}_0(\mathbf{s}_f)$, can be approximated using PO:

$$\mathbf{J}_0(\mathbf{s}_f) = 2\hat{\mathbf{n}} \times \mathbf{H}^i(\mathbf{s}_f) \tag{2.4}$$

where $\mathbf{H}^i$ is the incident magnetic field intensity. Assuming that f is many wavelengths long, the magnetic field intensity can be calculated using the plane wave relationship:

$$\mathbf{H}^i(\mathbf{s}_f) = \frac{\hat{\mathbf{s}}_f \times \mathbf{E}^i(\mathbf{s}_f)}{\eta} \tag{2.5}$$

where $\hat{\mathbf{s}}_f = \mathbf{s}_f/|\mathbf{s}_f|$. The unit vector normal at $\mathbf{s}_f$, $\hat{\mathbf{n}}$, is [13](Equation 9-188):

$$\hat{\mathbf{n}} = \frac{\rho\hat{\boldsymbol{\rho}} + 2f\hat{\mathbf{z}}}{\sqrt{4f^2 + \rho^2}} \tag{2.6}$$

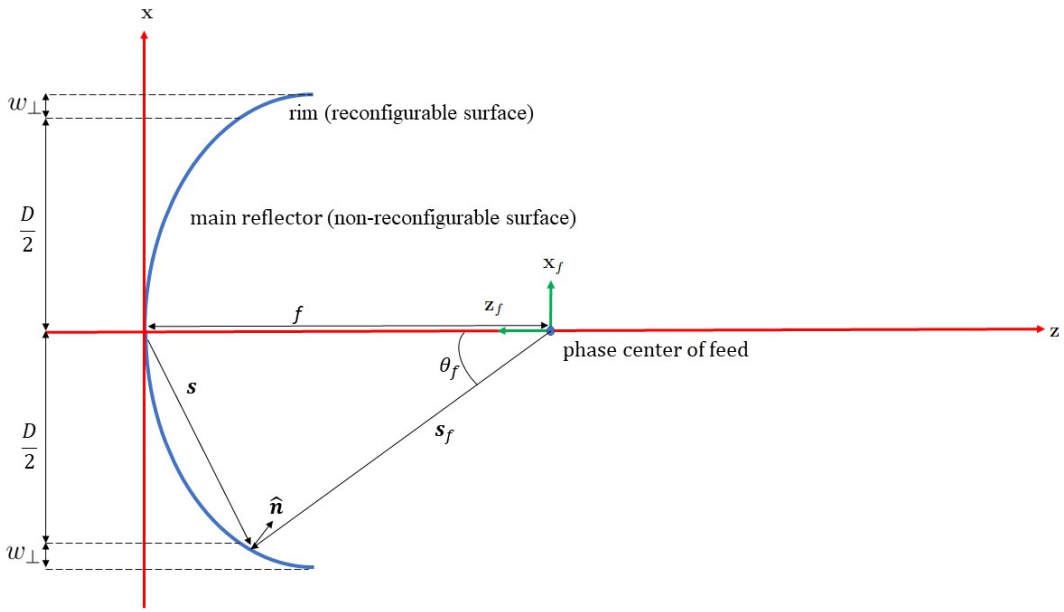

Figure 2.2: Cross-sectional view of the reflector system with reconfigurable surface on the rim of the reflector.

Then, $\mathbf{E}_0^s(\mathbf{r})$ can be calculated using the far-field radiation integral:

$$\mathbf{E}_0^s(\mathbf{r}) = -j\omega\mu\frac{e^{-j\beta r}}{4\pi r}\int_{\rho=0}^{D/2}\int_{\phi=0}^{2\pi}\mathbf{J}_0(\mathbf{s}_f)e^{j\beta\hat{\mathbf{r}}\cdot\mathbf{s}_f}ds \tag{2.7}$$

where $\mathbf{r} = r\hat{\mathbf{r}}$, r is the distance from O to the field point, β is the phase propagation constant ($\beta = 2\pi/\lambda$), and ds is the differential surface area [13](Equation 16-165):

$$ds = \frac{\sqrt{4f^2+\rho^2}}{2f}\rho\, d\rho\, d\phi \tag{2.8}$$

A closed-form solution for Equation 2.7 is typically not possible, therefore a numerical calculation is used:

$$\mathbf{E}_0^s(\mathbf{r}) \cong -j\omega\mu\frac{e^{-j\beta r}}{4\pi r}\sum_{m=1}^{M}\mathbf{J}_0[m]e^{j\beta\hat{\mathbf{r}}\cdot\mathbf{s}_f[m]}\Delta s[m] \tag{2.9}$$

where m indexes points on the reflector. To account for the discretization, the reflector surface will consist of a grid of cells whose area, Δs, is:

$$\Delta s = \frac{\sqrt{4f^2+\rho^2}}{2f}\rho\, \Delta\rho\, \Delta\phi \tag{2.10}$$

where $\Delta\phi$ and $\Delta\rho$ are the analogues of $d\phi$ and $d\rho$ on the non-reconfigurable portion of the reflector, respectively.

For PO, $\Delta\rho$ and Δs are chosen within the following range to give a reasonable trade-off between accuracy and computation time:

$$0.1\lambda \leq \Delta\rho \leq 0.4\lambda \tag{2.11}$$

$$0.01\lambda^2 \leq \Delta s \leq 0.16\lambda^2 \tag{2.12}$$

The specific values chosen in this study are described in Sections 3.3 and 3.4.

2.2.2 Reconfigurable Surface

The reconfigurable surface is modeled as a grid of approximately square cells, where each cell represents an element. The total scattered electric field from the reconfigurable portion of the reflector, $\mathbf{E}_r^s(\mathbf{r})$, is found by adapting Equation 2.9:

$$\mathbf{E}_r^s(\mathbf{r}) = -j\omega\mu\frac{e^{-j\beta r}}{4\pi r}\sum_{n=1}^{N}\mathbf{J}_r[n]e^{j\beta\hat{\mathbf{r}}\cdot\mathbf{s}_f[n]}\Delta s[n] \tag{2.13}$$

where N is the number of elements, and $\mathbf{J}_r[n]$ is the equivalent surface current density of the n^{th} cell. The gridding chosen for this study is described in Section 3.2. For this study, the length of each side of each cell is $\lambda/2$. Note that this is the expected size of one ERS element (see e.g., [7] and [12]). Thus, $\Delta s_r = \lambda/2 \times \lambda/2,\ \forall\ n$. As noted in Figure 2.2, we define the projected width from the edge of the non-reconfigurable portion of the reflector to the upper edge of the reconfigurable portion of the reflector as $w_\perp$.

As in [7], the surface equivalent current density at $\mathbf{s}_f[n]$ is assumed to be of the following form:

$$\mathbf{J}_r[n] = C_n\mathbf{J}_0[n] \tag{2.14}$$

where C_n is a constant that accounts for the reconfigurability (e.g. phase shifting) of the n^{th} ERS element.

2.3 Serial Search Algorithm for Nulling

The purpose of this section is to present a methodology for determining the states of the ERS elements in order to create a null in a given direction. This is the methodology proposed in [7].

Recall that the total scattered electric field from the reflector, in a given direction (θ_m, ϕ_m), is the sum of the scattered electric fields from both the non-reconfigurable ($\mathbf{E}_0^s$) and reconfigurable portions ($\mathbf{E}_r^s$) of the reflector:

$$\mathbf{E}^s(\mathbf{r}(\theta_m,\phi_m)) = \mathbf{E}_0^s(\mathbf{r}(\theta_m,\phi_m)) + \mathbf{E}_r^s(\mathbf{r}(\theta_m,\phi_m)) \tag{2.15}$$

This can be expanded using Equation 2.13:

$$\mathbf{E}^s(\mathbf{r}(\theta_m,\phi_m)) = \mathbf{E}_0^s(\mathbf{r}(\theta_m,\phi_m)) - j\omega\mu\frac{e^{-j\beta r}}{4\pi r}\sum_{n=1}^{N}\mathbf{J}_r[n]e^{j\beta\hat{\mathbf{r}}\cdot\mathbf{s}_f[n]}\Delta s[n] \tag{2.16}$$

Recall that $\mathbf{J}_r[n] = C_n\mathbf{J}_0[n]$ on the reconfigurable portion of the rim. The Q^{th} partial sum of $\mathbf{E}^s(\mathbf{r}(\theta_m,\phi_m))$ can be defined as:

$$\mathbf{E}_p^s(\mathbf{r}(\theta_m,\phi_m),Q) = \mathbf{E}_0^s(\mathbf{r}(\theta_m,\phi_m)) - j\omega\mu\frac{e^{-j\beta r}}{4\pi r}\sum_{n=1}^{Q}C_n\mathbf{J}_0[n]e^{j\beta\hat{\mathbf{r}}\cdot\mathbf{s}_f[n]}\Delta s[n] \tag{2.17}$$

where $Q = 1,\ 2, ...,\ N$. For nulling, the set of C_n values ($\mathbf{C}$) is chosen to minimize $|\mathbf{E}^s(\mathbf{r}(\theta_m,\phi_m))|$. One method used to determine $\mathbf{C}$ is the Serial Search Algorithm [7]. Essentially, the Serial Search Algorithm calculates the C_n which minimize $\left|\mathbf{E}_p^s(\mathbf{r}(\theta_m,\phi_m),Q)\right|$. Note that $\mathbf{J}_r[n]$ corresponds to C_n. To start, C_1 can be calculated such that $\left|\mathbf{E}_p^s(\mathbf{r}(\theta_m,\phi_m),Q=1)\right|$ is minimized:

$$\min\left|\mathbf{E}_p^s(\mathbf{r}(\theta_m,\phi_m),Q=1)\right| = \min\left|\mathbf{E}_0^s(\mathbf{r}(\theta_m,\phi_m)) - j\omega\mu\frac{e^{-j\beta r}}{4\pi r}C_1\mathbf{J}_0[1]e^{j\beta\hat{\mathbf{r}}\cdot\mathbf{s}_f[1]}\Delta s[1]\right| \tag{2.18}$$

Now, C_2 can be found using C_1:

$$\min\left|\mathbf{E}_p^s(\mathbf{r}(\theta_m,\phi_m),Q=2)\right| = \min\left|\mathbf{E}_p^s(\mathbf{r}(\theta_m,\phi_m),Q=1) - j\omega\mu\frac{e^{-j\beta r}}{4\pi r}C_2\mathbf{J}_0[2]e^{j\beta\hat{\mathbf{r}}\cdot\mathbf{s}_f[2]}\Delta s[2]\right| \tag{2.19}$$

Similarly, C_3 can be found using both C_2 and C_1:

$$\min\left|\mathbf{E}_p^s(\mathbf{r}(\theta_m,\phi_m),Q=3)\right| = \min\left|\mathbf{E}_p^s(\mathbf{r}(\theta_m,\phi_m),Q=2) - j\omega\mu\frac{e^{-j\beta r}}{4\pi r}C_3\mathbf{J}_0[3]e^{j\beta\hat{\mathbf{r}}\cdot\mathbf{s}_f[3]}\Delta s[3]\right| \tag{2.20}$$

This process continues until $Q = N$.

Unless otherwise specified, C_n is calculated starting from $\phi = 0$ to $\phi = 2\pi$ for increasing values of ρ from $D/2$ to $D/2 + w_\perp$.

2.4 Directivity and Pattern Characteristics

Three quantities are defined to assess the performance of the reflector system: Directivity, half-power beamwidth, and the first sidelobe level.

Directivity (G): The directivity is defined as the ratio of power density in a specified direction to the average power density over all directions at the same distance:

$$G(\hat{\mathbf{r}}) = \frac{S(\hat{\mathbf{r}}R)}{\langle S(\hat{\mathbf{r}}R)\rangle} \tag{2.21}$$

where $S(\hat{\mathbf{r}}R)$ is the power density at $\hat{\mathbf{r}}R$ and $\langle S(\hat{\mathbf{r}}R)\rangle$ is the power density averaged over a sphere of radius R. The power density at $\hat{\mathbf{r}}R$ can be calculated as:

$$S(\hat{\mathbf{r}}R) = \frac{|\mathbf{E}^s(\hat{\mathbf{r}}R)|^2}{2\eta} \tag{2.22}$$

In general, $\mathbf{E}^s(\hat{\mathbf{r}}R)$ is the sum of the electric field intensities from the reflector and the feed. However, we shall assume that the electric field in the half-space facing away from the feed pointing direction is negligible relative to the scattered electric field from the reflector. Thus, the electric field radiated by the system is assumed to consist of the scattered electric field from the reflector only. This is justified by the fact that the field scattered by the feed opposite of the feed pointing direction is orders of magnitude smaller than the field scattered by the reflector in this direction.

To find $\langle S(\hat{\mathbf{r}}R)\rangle$, the total power radiated, P_{rad}, is divided by the surface area of the sphere of radius R:

$$\langle S(\hat{\mathbf{r}}R)\rangle = \frac{P_{rad}}{4\pi R^2} \tag{2.23}$$

where P_{rad} can be found by integrating Equation 2.22 over the surface of the sphere:

$$P_{rad} = \int_{\theta=0}^{\pi}\int_{\phi=0}^{2\pi} S(\hat{\mathbf{r}}R)R^2 \sin\theta \; d\phi \; d\theta \tag{2.24}$$

Thus:

$$\langle S(\hat{\mathbf{r}}R)\rangle = \frac{1}{4\pi}\int_{\theta=0}^{\pi}\int_{\phi=0}^{2\pi} \frac{|\mathbf{E}^s(\hat{\mathbf{r}}R)|^2}{2\eta} \sin\theta \; d\phi \; d\theta \tag{2.25}$$

Equation 2.25 can be simplified by replacing $\mathbf{E}^s(\hat{\mathbf{r}}R)$ with $\mathbf{E}^i(\hat{\mathbf{r}}R)$. The reasoning follows from the conservation of power: The total power scattered from the system must be the same as the power from the feed. Therefore,

$$\langle S(\hat{\mathbf{r}}R)\rangle = \frac{1}{4\pi}\int_{\theta=0}^{\pi}\int_{\phi=0}^{2\pi} \frac{|\mathbf{E}^i(\hat{\mathbf{r}}R)|^2}{2\eta} \sin\theta \; d\phi \; d\theta \tag{2.26}$$

which yields the same result as Equation 2.25 but can be pre-computed since $\mathbf{E}^i(\hat{\mathbf{r}}R)$ is independent of the PO calculation.

Side Lobe Level (SLL): The SLL is defined as the directivity of the first sidelobe with respect to the directivity of the main lobe.

Half-Power Beamwidth (HPBW): The HPBW is defined as the angular span between the points on the main lobe that are half the maximum value of $G(\hat{\mathbf{r}}(\theta, \phi_c))$, where ϕ_c is the specific plane of interest.

It is useful to compare the performance of the reflector system to that of a planar uniformly illuminated circular aperture (UICA) of diameter D [13]. See Figure 2.3 for a UICA and a reflector of the same diameter. Note that the maximum directivity of UICA is an upper bound for a reflector of equivalent diameter. Additionally, the HPBW and SLL of a UICA provide an estimate to that of a reflector of equivalent diameter. The maximum directivity, HPBW, and SLL of a UICA are given by Equations 2.27-2.29, respectively, from [13]:

$$G = \left(\frac{\pi D}{\lambda}\right)^2 \tag{2.27}$$

$$\text{SLL} = -17.6 \text{ dB} \tag{2.28}$$

$$\text{HPBW} = \frac{1.02\lambda}{D} \text{ rad} \tag{2.29}$$

2.5 Polarization and Patterns

The co-polarized field (co-pol) is the component of $\mathbf{E}^s$ in the ideal or intended direction, and the cross-polarized field (cross-pol) is the component of $\mathbf{E}^s$ orthogonal to both the co-pol direction and direction of propagation. The magnitudes of these fields are:

$$\begin{aligned} E_{co} &\stackrel{\text{def}}{=} |\hat{\mathbf{e}} \cdot \mathbf{E}^s| \\ E_{cross} &\stackrel{\text{def}}{=} |\hat{\mathbf{h}} \cdot \mathbf{E}^s| \end{aligned} \tag{2.30}$$

Where $\hat{\mathbf{e}}$ is the co-pol unit vector, and $\hat{\mathbf{h}}$ is the cross-pol unit vector. Following common practice, $\hat{\mathbf{e}}$ is defined to be the same direction as the electric field radiated by a Huygens' source placed at O [14]. For a Huygens' source whose electric current moment is $\hat{\mathbf{y}}$-oriented, the co-pol and cross-pol vectors become:

$$\hat{\mathbf{e}} = \hat{\boldsymbol{\theta}} \sin\phi + \hat{\boldsymbol{\phi}} \cos\phi \tag{2.31}$$

$$\hat{\mathbf{h}} = \hat{\boldsymbol{\phi}} \sin\phi - \hat{\boldsymbol{\theta}} \cos\phi \tag{2.32}$$

Note that the H- and E-planes correspond to $\phi = 0$ and $\phi = \pi/2$ rad, respectively.

2.6 Feed Model

The feed model used exclusively throughout this thesis is a modified Huygens' source whose electric current is $\hat{\mathbf{y}}$-oriented. This section will develop the mathematical model of the feed used in this thesis.

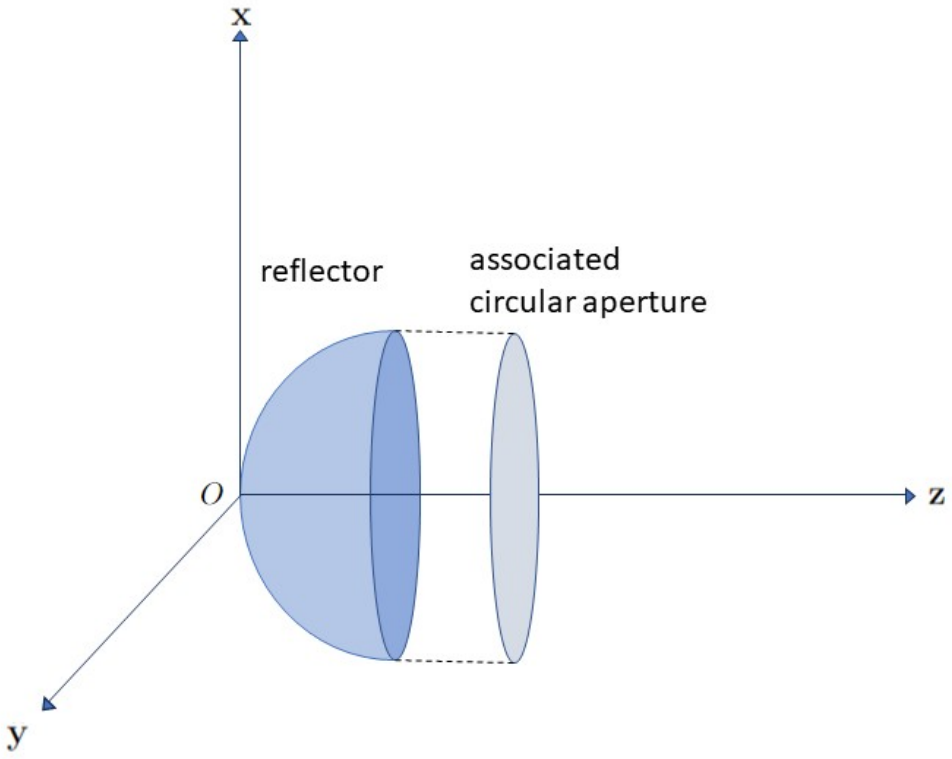

Figure 2.3: The reflector with the associated circular aperture. Note that for an axisymmetric circular reflector, the edge of the aperture is a circle.

Electric field from a Huygens' source: A Huygens' source can be modeled as an electrically-short electric dipole that is placed orthogonal to an electrically-short magnetic dipole. One form of the electric field from an unmodified Huygens' source is ([15], Equation 2.24):

$$\mathbf{E}^i(\mathbf{s}_f) = E_0(\hat{\mathbf{l}}_e \times \hat{\mathbf{s}}_f \times \hat{\mathbf{s}}_f + \hat{\mathbf{l}}_h \times \hat{\mathbf{s}}_f)\frac{e^{-j\beta s_f}}{s_f} \tag{2.33}$$

where $\hat{\mathbf{l}}_e$ and $\hat{\mathbf{l}}_h$ are the orientation of the electric and magnetic currents, respectively, and E_0 is a complex constant that accounts for the magnitude and phase of the source.

Electric field from a modified Huygens' source: For many practical applications, it is desired to control the taper of the electric field between the edge of the reflector relative to the vertex of the reflector. This is commonly referred to as the edge illumination (EI) and is fixed for a Huygens' source. To allow for the possibility of different EI's, Equation 2.33 is modified with a $\cos^q \theta_f$ factor:

$$\mathbf{E}^i(\mathbf{s}_f) = E_0\frac{(\hat{\mathbf{l}}_e \times \hat{\mathbf{s}}_f \times \hat{\mathbf{s}}_f + \hat{\mathbf{l}}_h \times \hat{\mathbf{s}}_f)}{|\hat{\mathbf{l}}_e \times \hat{\mathbf{s}}_f \times \hat{\mathbf{s}}_f + \hat{\mathbf{l}}_h \times \hat{\mathbf{s}}_f|}\cos^q \theta_f \frac{e^{-j\beta s_f}}{s_f} \tag{2.34}$$

The relationship between q, EI, and θ_0, the angle from the $+\hat{\mathbf{z}}_f$ axis to the rim of the reflector, is given by Equation 9-233 [13]:

$$\text{EI} = \left(\frac{1+\cos\theta_0}{2}\right)\cos^q \theta_0 \tag{2.35}$$

As mentioned in Section 2.4, the electric field in the half-space pointing away from the feed pointing direction is negligible. Hence,

$$\mathbf{E}^i(\mathbf{s}_f) = 0, \quad \theta_f \geq \pi/2 \tag{2.36}$$

Chapter 3

Implementation of the Physical Optics Model

The purpose of this chapter is to describe the method used to implement the theory from Chapter 2 to calculate the scattered electric field from the reflector system. The results from this chapter provide a baseline for comparison when assessing performance of the reflector system for subsequent chapters.

Sections 3.1 and 3.2 discuss the gridding of the non-reconfigurable and reconfigurable portions of the reflector, respectively. Sections 3.3 and 3.4 provides an evaluation of a reflector system with and without a reconfigurable surface, respectively.

3.1 Gridding the Non-Reconfigurable Portion of the Reflector

The purpose of this section is to appropriately size the cell dimensions of the non-reconfigurable portion of the reflector, as shown in Figure 3.1. Since there are two sets of gridding (one for the non-reconfigurable and reconfigurable portions of the reflector), we designate the subscript 0 and r to indicate the gridding of the non-reconfigurable and reconfigurable portions of the reflector, respectively. Thus, $\Delta\rho_0 \rightarrow \Delta\rho$ and $\Delta\phi_0 \rightarrow \Delta\phi$ on the non-reconfigurable portion of the reflector.

Note that there are two different kinds of cells on the non-reconfigurable portion of the reflector: A single, circular vertex cell at the center of the reflector and the non-vertex cells elsewhere. The non-vertex cells will be approximately square on the rim such that:

$$\frac{D}{2}\Delta\phi_0 = \Delta\rho_0 \tag{3.1}$$

thus

$$\Delta\phi_0 = \frac{\Delta\rho_0}{D/2} \tag{3.2}$$

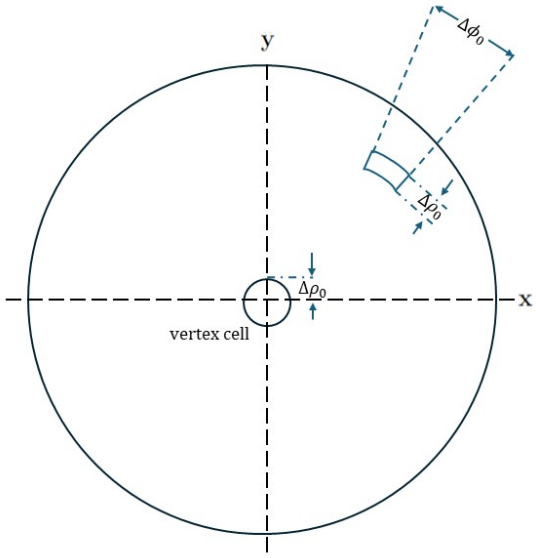

Figure 3.1: Front view of reflector to show gridding of the reflector.

For the vertex cell, the radius is chosen to be $\Delta\rho_0$.

3.2 Gridding the Reconfigurable Portion of the Reflector

The purpose of this section is to appropriately size the cell dimensions of the reconfigurable portion of the reflector. As described in Section 3.1, the arc length of each cell is desired to be $\lambda/2$ in length. Thus, $\Delta\rho_r$, the analogue of $\Delta\rho_0$ on the reconfigurable portion of the reflector, is chosen to be:

$$\Delta\rho_r = \frac{\lambda}{2} \tag{3.3}$$

For the arc length of each side of the cell to be equal to $\lambda/2$, the radial arc length must equal to:

$$\rho\Delta\phi_r = \frac{\lambda}{2} \tag{3.4}$$

Thus,

$$\Delta\phi_r = \frac{\lambda}{2\rho} \tag{3.5}$$

Variable	Value
Frequency	1.5 GHz
f/D	0.35
D	102λ
q	1.14

Table 3.1: Design parameters for the example of Section 3.3.

	Case 1	Case 2	Case 3
$\Delta\rho_0$	0.4λ	$0.3\ \lambda$	$0.2\ \lambda$
$\Delta\phi_0$	0.50°	0.40°	0.30°
Largest Cell Size	$0.4\lambda \times 0.4\lambda$ ($0.16\ \lambda^2$)	$0.3\lambda \times 0.3\lambda$ ($0.09\ \lambda^2$)	$0.2\lambda \times 0.2\lambda$ ($0.04\ \lambda^2$)
G	49.00 dBi	49.10 dBi	49.10 dBi
SLL	28.05 dB	28.90 dB	28.90 dB
HPBW	0.80°	0.80°	0.80°
Computation Time	8.80 min	1.24 min	0.56 min

Table 3.2: Results for the example in Section 3.3.

Note that $\Delta\phi_r$ must vary according to ρ to maintain the $\lambda/2 \times \lambda/2$ cell dimensions. Since the circumference will not be an integer multiple of wavelengths, this will create gaps between the cells. Since the overall gap length is small compared to the circumference, the gaps will not significantly affect $\mathbf{E}^s$ and can be neglected. Previous work on this matter has been addressed in [12], and this assumption is accurate.

3.3 Example Calculation: Traditional System

In this section, a non-reconfigurable reflector will be analyzed to determine an appropriate grid cell size. The reflector system uses a Huygens' source feed with design parameters shown in Table 3.1. For this study, three grid cell sizes will be considered.

The results of this study are shown in Table 3.2. Among Cases 1-3, Case 1 differs significantly from Cases 2 and 3 in terms of the G, SLL, and HPBW. Thus, it can be concluded that the grid size for Case 1 is too coarse. On the other hand, there is no significant difference in G, SLL, and HPBW between Cases 2 and 3. The grid size will be chosen according to Case 2 since it has a shorter computational time.

Figure 3.2 shows the co-pol directivity for the selected gridding. To further validate the calculations, we compare the previous results to a UICA of the same diameter as described in Section 2.4. The results of this comparison are shown in Table 3.3. Note that the directivity using PO is about 1 dB lower than that of the UICA's. This indicates that the reflector system has an aperture efficiency of 79.4%. Additionally, the SLL for the result using PO is

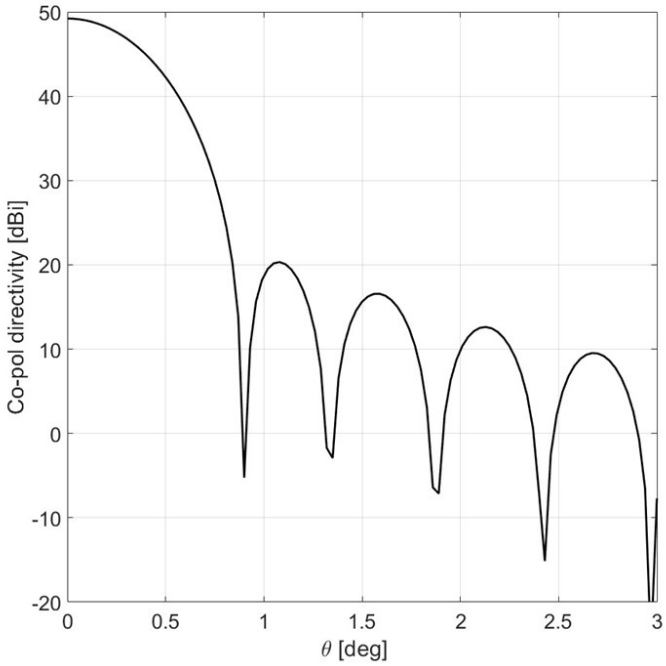

Figure 3.2: H-plane co-polarized pattern of the example in Section 3.3.

	PO	UICA
G	49.10 dBi	50.01 dBi
HPBW	0.80°	0.70°
SLL	28.90 dB	17.60 dB

Table 3.3: Results for the example in Section 3.3.

much greater than the UICA's, which is expected for a practical reflector. Lastly, note that the HPBW for both cases are approximately the same. This is expected, as the width of the main lobe is generally determined by the size of the aperture (Chapter 9.5)[13].

3.4 Example Calculation: Reconfigurable System

In this section, we will analyze a reflector with a reconfigurable rim with the desired null located at $(\theta_m, \phi_m) = (1.75°, 0)$. Note that the choice of (θ_m, ϕ_m) is the location of peak of the second sidelobe of a 90λ diameter reflector, where $\lambda = 0.2$ m (see e.g., [7] and [8]). The results from this study will serve as a baseline comparison for the examples in Chapters 4 and 5. The parameters of the reflector system are shown in Table 3.4.

Three results are compared in this study: (1) When the ERS is in the Quiescent state (i.e., $C_n = 1, \ \forall \ n$), (2) When the ERS is configured to null at (θ_m, ϕ_m), and (3) The results

	Variable	Value
Reflector System Parameters	Frequency	1.5 GHz
	f/D	0.42
	D	90λ
	q	1.14
	$w_\perp$	6λ
Nulling Direction	θ_m	1.75°
	ϕ_m	0
Analysis Parameters	$\Delta\rho_0$	$0.3\ \lambda$
	$\Delta\phi_0$	0.40°
	$\Delta\rho_r$	$0.5\ \lambda$
	Range of $\Delta\phi_r$	$0.56^\circ - 0.64^\circ$

Table 3.4: Parameters for the example in Section 3.4. Note that $q = 1.14$ corresponds to EI $= -11$ dB for a reflector with $D = 18$ m.

	Section 3.3	ERS, quiescent state	ERS, nulling
G	49.10 dBi	48.89 dBi	48.20 dBi
HPBW	0.80°	0.80°	0.80°
SLL	28.90 dB	27.61 dB	27.01 dB

Table 3.5: Results for Section 3.4.

from the analysis of the non-reconfigurable reflector from Section 3.3. The H-plane co-pol patterns are shown in Figure 3.3, and the results are summarized in Table 3.5. The state of each ERS element in the nulling state is shown in Figure 3.4 as the "First Order", where $\mathbf{C}$ is calculated as described in Section 2.3. For the Quiescent and Nulling cases, the main lobe directivity drops by 0.21 dB and 0.90 dB compared to the non-reconfigurable system from Section 3.3, respectively. Compared to the non-reconfigurable reflector, SLL decreases by 1.29 dB and 1.89 dB for the quiescent and nulling states, respectively.

Note that $\mathbf{C}$ changes depending on the order in which the state vector is calculated. As an example, see "Second Order" in Figure 3.4 for an inset diagram of $\mathbf{C}$, where C_n is calculated starting from $\rho = D/2$ to $\rho = D/2 + w_\perp$ for increasing values of ϕ from 0 to 2π. The pattern is calculated using the "Second Order" and compared to the pattern calculated using the "First Order", with the results shown in Table 3.6. Although there are differences in the peak cross-pol and null depth, the G, HPBW, and SLL remain virtually the same. Since the SSA has no constraints other than to drive a null, this difference in the null depth and peak cross-pol is plausible. For the remainder of this thesis, we will use the "First Order" to calculate $\mathbf{C}$.[1]

[1]Future work could focus on studying the effects on the cross-pol and null depth as a function of the order in which $\mathbf{C}$ is calculated.

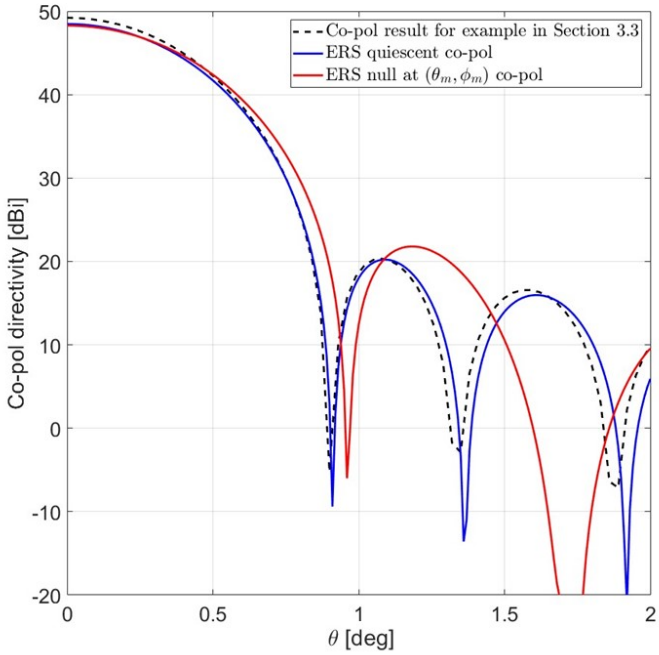

Figure 3.3: H-plane pattern results for the example in Section 3.4 compared to the results in Section 3.3.

	First Order	Second Order
G	48.20 dBi	48.21 dBi
HPBW	0.80°	0.78°
SLL	27.01 dB	26.99 dB
Peak XPOL	−44.00 dBi	−50.01 dBi
Null Depth	−65.20 dBi	−55.02 dBi

Table 3.6: Results for comparing the two different orders of $\mathbf{C}$ for Section 3.4, where "XPOL" is the cross-pol magnitude.

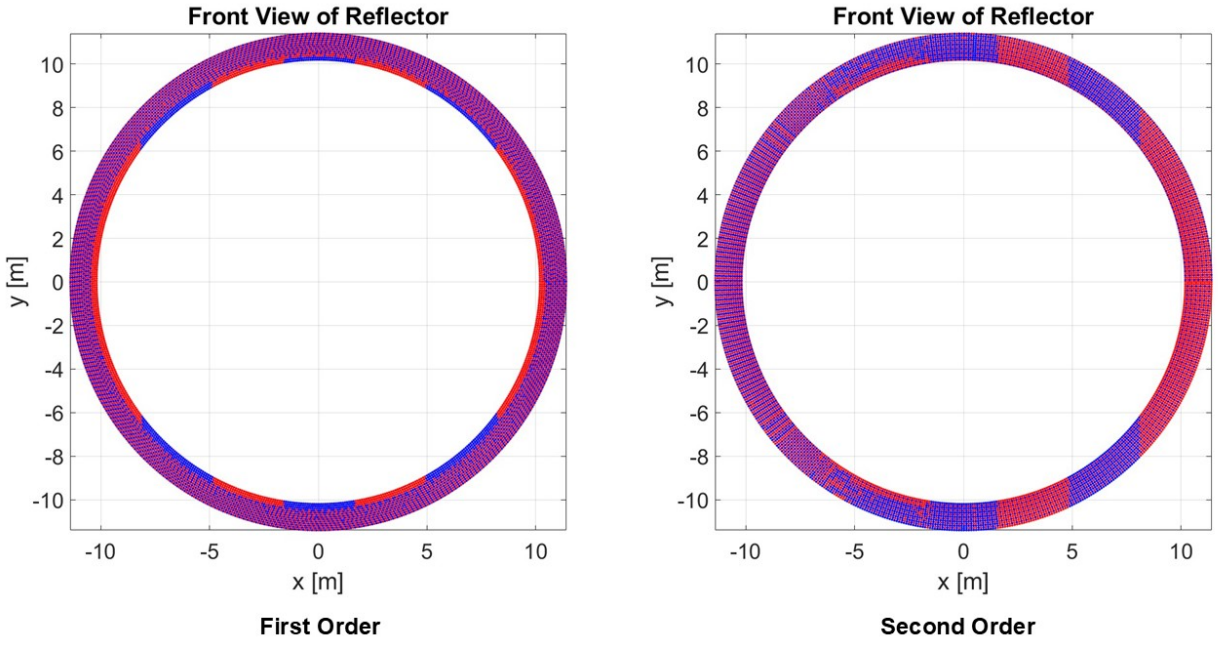

Figure 3.4: Front view of reconfigurable surface for the examples in Section 3.4 where the state vectors are color-coded with red corresponding to $C_n = +1$, and blue corresponding to $C_n = -1$. *Left:* $\mathbf{C}$ is calculated from $\phi = 0$ to $\phi = 2\pi$ for increasing values of ρ from $D/2$ to $D/2 + w_\perp$. *Right:* $\mathbf{C}$ is calculated from $\rho = D/2$ to $\rho = D/2 + w_\perp$ for increasing values of ϕ from 0 to 2π.

3.5 Conclusions

This chapter provided two results for the scattered electric field calculated using PO: One for a system with no reconfigurable surface, and one for a system with a reconfigurable surface on the rim of the reflector. The first result will be used in Chapter 4 to validate an approximation for the scattered electric field from a reflector system. The second result will serve as a baseline comparison of the outrigger panel systems that are explored in Chapter 5.

Chapter 4

Determining the Width of the ERS Rim

4.1 Introduction

It is desired to determine the minimum width of the ERS, $w_{\perp,min}(m)$, that allows nulling over the entire m^{th} sidelobe of the pattern of the non-reconfigurable portion of a reflector system, given only f/D and a simple parametric description of the feed. When $w_\perp = w_{\perp,min}(m)$, the co-polarized magnitude of $\mathbf{E}_0^s(\mathbf{r})$ (the electric field scattered from the ERS at $\mathbf{r}$) is equal to the co-polarized magnitude of $\mathbf{E}_r^s(\mathbf{r})$ (the electric field scattered from the central non-reconfigurable portion of the reflector at $\mathbf{r}$) at the peak of the m^{th} sidelobe of the pattern associated with $\mathbf{E}_0^s(\mathbf{r})$. In principle, this value of $w_\perp$ can be determined directly by comparing the maximum possible magnitude of $\mathbf{E}_r^s(\mathbf{r})$ to that of $\mathbf{E}_0^s(\mathbf{r})$ while varying $w_\perp$, using PO. However, this requires iteration over $w_\perp$, with each step in the iteration requiring an integration over the ERS. In contrast, this chapter presents a method for approximating $w_{\perp,min}(m)$ that does not require PO integration nor iteration. This method is useful for first-pass design of ERS-equipped reflector systems and for gaining insight into the relative effects of the various design parameters.

The organization of this chapter is as follows: An approximate, closed form expression for $\mathbf{E}_0^s(\mathbf{r})$ and $\mathbf{E}_r^s(\mathbf{r})$ is developed in Sections 4.2 and 4.3, respectively. In Section 4.4, an expression to determine the peak of the m^{th} sidelobe is derived. From these results, an approximate closed form expression for $w_{\perp,min}$ is derived in Section 4.5. This chapter is summarized in Section 4.6 followed by a demonstration of the calculation of $w_{\perp,min}$.

4.2 Approximate Calculation of $\mathbf{E}_0^s$

The method used to estimate $\mathbf{E}_0^s(\mathbf{r})$ is adapted from [15], which is an extension of the theory presented in [13]. Here is a brief description of the method: Within the first few sidelobes, $\mathbf{E}_0^s(\mathbf{r})$ is well-modeled as the radiation from a circular planar aperture bounding an electric

field $\mathbf{E}_a(\mathbf{r}')$ representing the collimated geometrical optics field from the reflector. This concept is illustrated in Figure 4.1.

If a $\hat{\mathbf{y}}$ (linearly) polarized balanced feed is assumed, and there is ideal polarization matching between feed and reflector, then $\mathbf{E}_a(\mathbf{r}') = \hat{\mathbf{y}} E_a(\rho')$, with no dependence on ϕ'. In this case, the radiated field is ([13], Sec 9.5):

$$\mathbf{E}_0^s(\mathbf{r}) \approx j\beta \frac{e^{-j\beta r}}{2\pi r} P_y(\theta,\phi) \left(\hat{\theta} \sin\phi + \hat{\phi} \cos\phi \cos\theta \right) \tag{4.1}$$

where

$$P_y(\theta,\phi) = \int_{\mathcal{S}} E_a(\rho') \; e^{+j\beta \hat{\mathbf{r}}\cdot\mathbf{r}'} ds' \tag{4.2}$$

where $\mathcal{S}$ denotes the aperture and ds' is the differential element of area within the aperture.

For example, for the UICA considered in previous chapters, $E_a(\rho') = E_0$ (a constant) which leads to

$$P_y(\theta,\phi) = E_0 A \left[\frac{2J_1\left(\beta\,(D/2)\sin\theta\right)}{\beta\,(D/2)\sin\theta} \right] \tag{4.3}$$

where $A = \pi\,(D/2)^2$ is the area of the aperture and J_1 is the first-order Bessel function of the first kind. Thus, $P_y(\theta,\phi)$ from Equation 4.3 substituted into Equation 4.1 yields an approximate closed form expression for $\mathbf{E}_0^s(\mathbf{r})$ applicable to the special case of ideal illumination of the reflector.

Returning to the general case, Equation 4.1 may be rewritten as follows:

$$\mathbf{E}_0^s(\mathbf{r}) \approx j\beta \frac{e^{-j\beta r}}{2\pi r} E_0 A f(\theta) \left(\hat{\theta} \sin\phi + \hat{\phi} \cos\phi \cos\theta \right) \tag{4.4}$$

where $f(\theta)$ is the real-valued "normalized pattern function". In this case "normalized" means having maximum value equal to 1. For example, for the UICA:

$$f(\theta) = \frac{2J_1\left(\beta\,(D/2)\sin\theta\right)}{\beta\,(D/2)\sin\theta} \tag{4.5}$$

For Equation 4.4 to accurately represent a reflector system with a practical feed, $f(\theta)$ must be determined using an appropriate model for $E_a(\rho')$. Such a model is the "parabolic taper on a pedestal" model from [13] (Table 9-2b). In this model,

$$\frac{E_a(\rho')}{E_0} = \mathrm{EI} + (1 - \mathrm{EI}) \left[1 - \left(\frac{\rho'}{D/2} \right)^2 \right]^n \tag{4.6}$$

This function decreases from 1 at the center ($\rho' = 0$) to EI (edge illumination[1]) at the rim of the non-reconfigurable portion of the reflector ($\rho' = D/2$). Note that $n = 0$ corresponds to the UICA, whereas larger values of n correspond to reflectors illuminated by practical feeds

[1] EI is denoted "C" in [13] and [15].

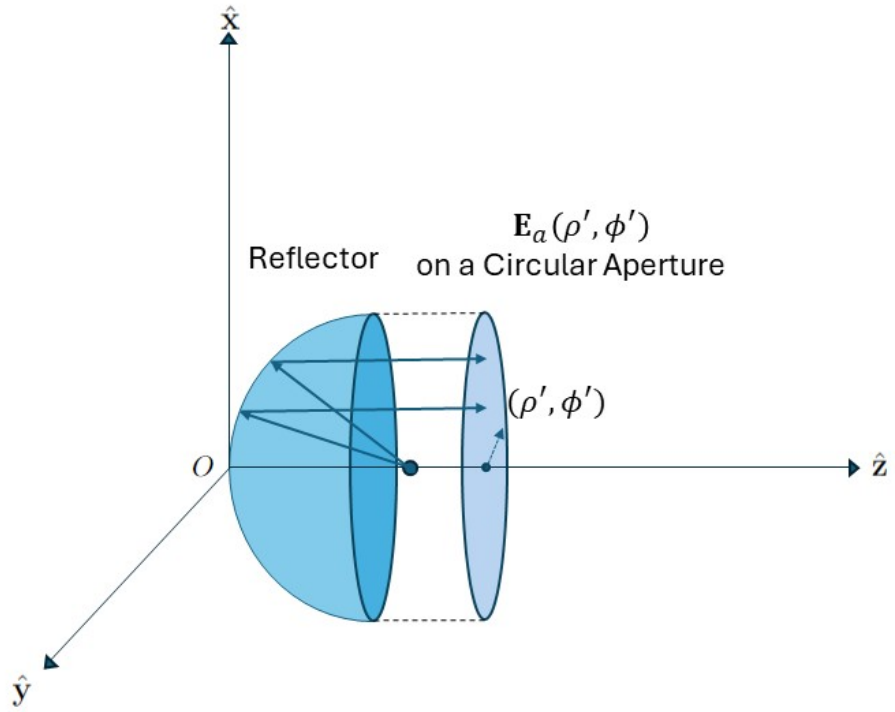

Figure 4.1: Radiating aperture model for $\mathbf{E}_0^s(\mathbf{r})$. Two geometrical optical rays which originate from the feed, reflect off of the reflector's surface, and terminate at the aperture plane.

having increasing directivity. This aperture distribution yields ([13], Table 9-2b.):

$$f(\theta) = F(\theta, \mathrm{EI}, n) = \frac{F(\theta, n=0) \cdot \mathrm{EI} + F(\theta, n) \cdot (1 - \mathrm{EI})/(n+1)}{\mathrm{EI} + (1 - \mathrm{EI})/(n+1)} \tag{4.7}$$

where

$$F(\theta, n) = \frac{2^{n+1} \cdot (n+1)! \cdot J_{n+1}(\beta(D/2)\sin\theta)}{(\beta(D/2)\sin\theta)^{n+1}} \tag{4.8}$$

and it is presumed in [13] that only integer values of n are valid.

While this is a step in the right direction, it is not clear how to choose n to correspond to the particular reflector system of interest, and [13] has nothing further to say on this issue. This matter was taken up in [15], where it is shown that a suitable value of n can be determined if the feed is well-described by the "$\cos^q$" model described in Section 2.6. In this case, n can be determined from f/D and either EI or q using the following procedure:

1. Calculate either EI (if q is provided) or q (if EI is provided) using the relationship ([13], Equation 9-233)
$$\mathrm{EI} = \left(\frac{1 + \cos\theta_0}{2}\right) \cos^q \theta_0 \tag{4.9}$$

2. Calculate the taper efficiency ϵ_t from the spillover efficiency ϵ_s and aperture efficiency ϵ_{ap}. This can be done by computing the following in sequence ([13], Equation 9-230; [15], Equation 4-16):
$$\epsilon_s = 1 - \cos^{2q+1}\theta_0 \tag{4.10}$$
$$\epsilon_{ap} = 2(2q+1)\left(\cot^2\frac{\theta_0}{2}\right)\left|\int_{\theta_f=0}^{\theta_0} \cos^q\theta_f \tan\frac{\theta_f}{2}\, d\theta_f\right|^2 \tag{4.11}$$
$$\epsilon_t = \frac{\epsilon_{ap}}{\epsilon_s} \tag{4.12}$$

3. Solve (numerically) the following equation ([13], Equation 9-181) for n:
$$\epsilon_t = \frac{[\mathrm{EI} + (1 - \mathrm{EI})/(n+1)]^2}{\mathrm{EI}^2 + 2 \cdot \mathrm{EI} \cdot (1 - \mathrm{EI})/(n+1) + (1 - \mathrm{EI})^2/(2n+1)} \tag{4.13}$$

This procedure typically yields a non-integer value of n, contrary to the integer value presumed in [13] and specifically by Equation 4.8. The generalized form of this equation suitable for non-integer values of n (as reported in [15]) is:

$$F(\theta, n) = \frac{2^{n+1}\Gamma(n+2)\ J_{n+1}(\beta(D/2)\sin\theta)}{(\beta(D/2)\sin\theta)^{n+1}} \tag{4.14}$$

where $\Gamma(\cdot)$ is the Gamma function. Note that $\Gamma(n) = (n+1)!$ as expected for integer values of n.

Variable	Value
f/D	0.40
D	90λ
q	1.14
$w_\perp$	6λ
Frequency	1.5 GHz

Table 4.1: Parameters for the example in Section 4.2. Note that $q = 1.14$ corresponds to EI $= -11$ dB for a reflector with $D = 90\lambda$, where $\lambda = 0.2$ m.

	PO integration (Sec 3.3)	Aperture plane approximation (Sec 4.2)
G	49.10 dBi	49.19 dBi
HPBW	0.80°	0.80°
SLL	28.90 dB	26.81 dB

Table 4.2: Summary of Figure 4.2.

Summarizing, $\mathbf{E}_0^s(\mathbf{r})$ is approximated using Equation 4.4 with normalized pattern function $f(\theta)$ from Equation 4.7, and $F(\theta, n)$ from Equation 4.14. Using Equations 4.9–4.13 (Steps 1–3 of the procedure reported above), n is determined. This procedure is appropriate for any circular axisymmetric paraboloidal reflector illuminated by a balanced "$\cos^q$" feed, and requires only f/D and either EI or q as input.

To demonstrate the accuracy of this method, consider Figure 4.2 which shows the directivity pattern of the approximation for the parameters in Table 4.1. Shown for comparison is the same pattern computed using PO in the manner of Section 3.3, for the same system. As indicated in Table 4.2, the agreement is excellent.

4.3 Approximate Calculation of $\mathbf{E}_r^s$

An expression for the maximum possible ("maximum magnitude") electric field that can be scattered from an ERS of width $w_\perp$ is desired. In principle, this requires the knowledge of the specific state vector $\mathbf{C}(\theta)$ that maximizes this field in each direction θ. This is a problem because there is no known way to anticipate this value of $\mathbf{C}(\theta)$; at present, this can be determined only by a numerical search.

However, $\mathbf{C}(\theta = 0)$ is known: This is simply the quiescent state of the ERS. In other words: For $C_n(\theta) = 1 \ \forall \ n$, the ERS behaves as a continuation of the non-reconfigurable portion of the reflector. Thus, the *total* field $\mathbf{E}^s(\theta = 0)$ can be calculated as the field scattered by a traditional (non-reconfigurable) reflector having the same diameter $D + 2w$ as the original (non-reconfigurable portion + ERS) reflector. Furthermore, $\mathbf{E}^s(\theta = 0)$ resulting from this model can be estimated using the same procedure described in Section 4.2.

Also, it is known that in the special case the C_n's are unit-magnitude with continuously-

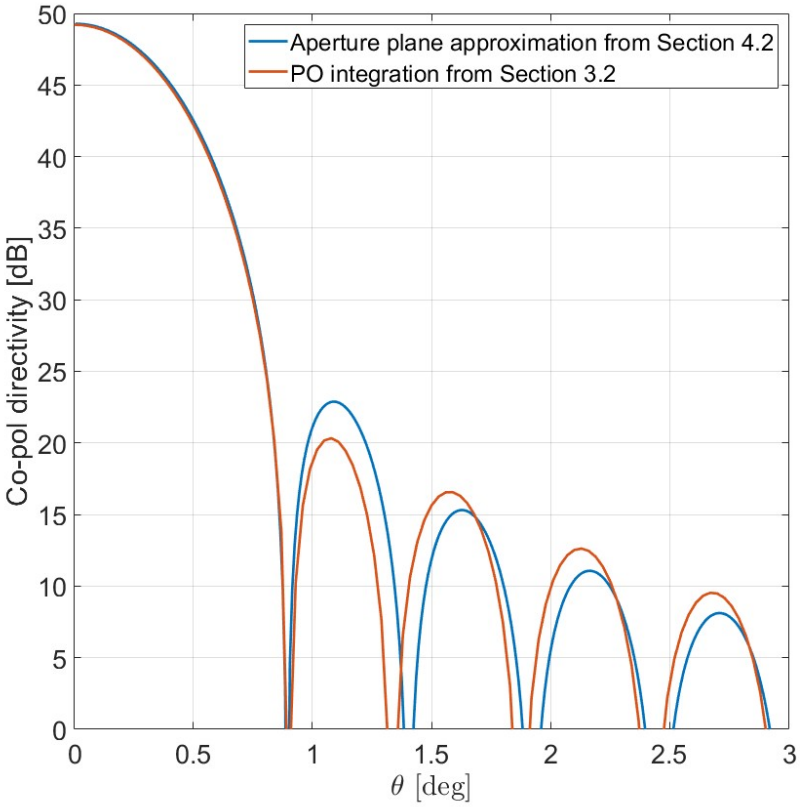

Figure 4.2: Comparison of PO integration (Section 3.3) and aperture plane approximation (Section 4.2) with parameters in Table 4.1.

variable phase, the variation in the maximum-magnitude value of $\mathbf{E}_r^s$ is negligible over the angular range containing the first few sidelobes. This is demonstrated in [7] (Figure 4).[2] For the approximation to be validated later in this section, it is assumed that the maximum-magnitude value of $\mathbf{E}_r^s(\mathbf{r}(\theta,\phi,r))$ is equal to $\mathbf{E}_r^s(\mathbf{r}(\theta=0,\phi,r))$ over the first few sidelobes of $\mathbf{E}_0^s(\mathbf{r})$.

These ideas can be combined as follows: Let $\mathbf{E}_{0+}^s(\mathbf{r})$ be the field scattered by a non-reconfigurable reflector having diameter $D+2w_\perp$, representing the original reflector consisting of a non-reconfigurable reflector of (smaller) diameter D plus an ERS in its quiescent state. In this situation:

$$\mathbf{E}_{0^+}^s(\mathbf{r}) = \mathbf{E}_0^s(\mathbf{r}) + \mathbf{E}_r^s(\mathbf{r}) \tag{4.15}$$

and so

$$\mathbf{E}_r^s(\mathbf{r}) = \mathbf{E}_{0^+}^s(\mathbf{r}) - \mathbf{E}_0^s(\mathbf{r}) \tag{4.16}$$

An expression for $\mathbf{E}_0^s(\mathbf{r})$ is available via the procedure of Section 4.2, which for later convenience is now written in the following form:

$$\mathbf{E}_0^s(\mathbf{r}) \approx j\beta\frac{e^{-j\beta r}}{2\pi r}E_0 AF(\theta,\mathrm{EI},n)\left(\hat{\theta}\sin\phi+\hat{\phi}\cos\phi\cos\theta\right) \tag{4.17}$$

To obtain an expression for $\mathbf{E}_{0^+}^s(\mathbf{r})$, the procedure of Section 4.2 will be employed here, with the following modifications:

- θ_0 becomes θ_{0+}, which is the angle to the edge of a traditional (non-reconfigurable) reflector of diameter $D+2w_\perp$.
- EI becomes EI_{0+}, which is the edge illumination for this reflector. Since the feed parameter q has not changed, Equation 4.9 (with θ_{0+} in lieu of θ_0) can be used to compute EI_{0+}.
- The parameter n becomes n_{0+}, which is computed as before, except with the appropriate changes of variable.
- The area A becomes

$$A_{0+} = \pi\left(\frac{D+2w_\perp}{2}\right)^2 \tag{4.18}$$

Thus,

$$\mathbf{E}_{0+}^s(\mathbf{r}) \approx j\beta\frac{e^{-j\beta r}}{2\pi r}E_0 A_{0+} F(\theta,\mathrm{EI}_{0+},n_{0+})\left(\hat{\theta}\sin\phi+\hat{\phi}\cos\phi\cos\theta\right) \tag{4.19}$$

and subsequently

$$\mathbf{E}_r^s(\mathbf{r}) \approx j\beta\frac{e^{-j\beta r}}{2\pi r}E_0\left[A_{0+}F(\theta,\mathrm{EI}_{0+},n_{0+}) - AF(\theta,\mathrm{EI},n)\right]\left(\hat{\theta}\sin\phi+\hat{\phi}\cos\phi\cos\theta\right) \tag{4.20}$$

[2]Figure 4 of [7] further demonstrates that the variation is quite small even if phases of the C_n's are quantized 1-bit quantities, albeit with a magnitude penalty of about 1 dB. For 2-bit phase quantization, the penalty varies between about 3 dB and 5 dB.

Following the reasoning presented earlier, the desired *maximum-magnitude* value of $\mathbf{E}_r^s(\mathbf{r})$, valid for values of θ covering the first few sidelobes, is given by the above expression evaluated with $\theta = 0$ in the relevant magnitude terms. That is:

$$\mathbf{E}_r^s(\mathbf{r}) \approx j\beta \frac{e^{-j\beta r}}{2\pi r} E_0 \left[A_{0+} F(\theta = 0, \mathrm{EI}_{0+}, n_{0+}) - AF(\theta = 0, \mathrm{EI}, n)\right] \left(\hat{\theta} \sin\phi + \hat{\phi} \cos\phi\right) \quad (4.21)$$

Further simplification is possible by noting that the functions $F(\cdot)$ are equal to 1 at $\theta = 0$; thus,

$$\mathbf{E}_r^s(\mathbf{r}) \approx j\beta \frac{e^{-j\beta r}}{2\pi r} E_0 \left[A_{0+} - A\right] \left(\hat{\theta} \sin\phi + \hat{\phi} \cos\phi\right) \quad (4.22)$$

Once again, this is an estimate of $\mathbf{E}_r^s(\mathbf{r})$ obtained when $\mathbf{C}(\theta)$ is optimized in the particular direction θ being considered; in contrast to the previous expression, which is an estimate of $\mathbf{E}_r^s(\mathbf{r})$ when $\mathbf{C}$ is optimized for $\theta = 0$ and then held fixed.

Following the design parameters from Table 4.1, the maximum magnitude of $|\mathbf{E}_r^s(\mathbf{r})|^2$ is calculated using Equation 4.22. This result is compared to the $|\mathbf{E}_r^s(\mathbf{r})|^2$ calculated using PO for 1-bit, 2-bit, and continuous-phase variation. The results are shown in Figure 4.3. Note that the result using Equation 4.22 is within 0.2 dB of the result using PO and continuous phase variation. Hence, the approximation for $\mathbf{E}_r^s(\mathbf{r})$ is justified.

Finally, note that for 1- and 2-bit phase variation, the maximum magnitude of $\mathbf{E}_r^s(\mathbf{r}(\theta, \phi, r))$ does not equal to $\mathbf{E}_r^s(\mathbf{r}(\theta = 0, \phi, r))$ over the first few sidelobes of $\mathbf{E}_0^s(\mathbf{r})$. In other words, the approximation for $w_{\perp,min}$ is inaccurate for coarse phase quantization. This is further explained in detail in Section 4.5.

4.4 Location of the Peak of the m^{th} Sidelobe of $\mathbf{E}_0^s$

In order to determine the width of the ERS required to yield $\mathbf{E}_r^s(\mathbf{r})$ of sufficient magnitude to cancel $\mathbf{E}_0^s(\mathbf{r})$ over the entire angular span of m^{th} sidelobe, it is necessary to know $\mathbf{E}_0^s(\mathbf{r}(\theta = \theta_m, \phi, r))$; i.e,, the field scattered from the non-reconfigurable portion of the reflector in the direction in which this magnitude is greatest. Because the value $\theta = \theta_m$ corresponds to the peak of the m^{th} sidelobe of $\mathbf{E}_0^s(\mathbf{r})$, it must be true that

$$\frac{\partial}{\partial\theta} \left|\mathbf{E}_0^s(\mathbf{r})\right|_{\theta=\theta_m} = 0 \quad (4.23)$$

Applying Equation 4.17, we obtain:

$$\frac{\partial}{\partial\theta} F(\theta, \mathrm{EI}, n)\bigg|_{\theta=\theta_m} = 0 \quad (4.24)$$

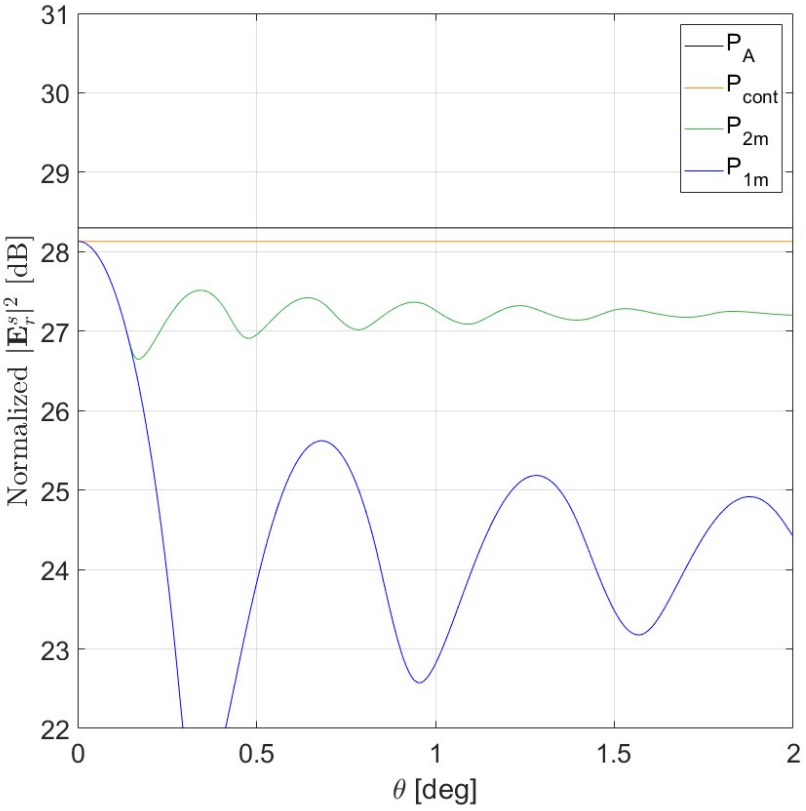

Figure 4.3: Comparison of $|\mathbf{E}_r^s(\mathbf{r})|^2$ using PO for 1-bit, 2-bit, and continuous phase variation (P_{1m}, P_{2m}, and P_{cont}, respectively) against the maximum magnitude of $|\mathbf{E}_r^s(\mathbf{r})|^2$ from Section 4.3 (P_A).

Applying Equation 4.7, we obtain:

$$\left[\mathrm{EI}\cdot\frac{\partial}{\partial\theta}F(\theta,n=0)+\frac{1-\mathrm{EI}}{n+1}\cdot\frac{\partial}{\partial\theta}F(\theta,n)\right]_{\theta=\theta_m}=0 \tag{4.25}$$

Note

$$\frac{\partial}{\partial\theta}F(\theta,n)=\frac{\beta(D/2)\cos\theta(\beta a\sin(\theta)J_0(\beta(D/2)\sin\theta)-2J_1(\beta(D/2)\sin\theta))}{(\beta(D/2)\sin\theta)^2} \tag{4.26}$$

The desired value, θ_m, can be obtained by numerical solution of Equation 4.25 with the assistance of Equation 4.26.

4.5 Estimation of $w_{\perp,min}$

Following the reasoning presented in the previous sections, $w_{\perp,min}(m)$ is defined by the condition

$$|\mathbf{E}_r^s(\mathbf{r}(\theta=\theta_m,\phi,r))|=|\mathbf{E}_0^s(\mathbf{r}(\theta=\theta_m,\phi,r))| \tag{4.27}$$

where $\mathbf{E}_r^s$ and $\mathbf{E}_0^s$ are given by Equations 4.22 and 4.17, respectively. Making the substitutions and eliminating common factors, we obtain:

$$A_{0+}-A=AF(\theta=\theta_m,\mathrm{EI},n) \tag{4.28}$$

Substituting for A_{0+} and A, we have

$$\pi\left(\frac{D+2w_{\perp,min}(m)}{2}\right)^2-\pi\left(\frac{D}{2}\right)^2=\pi\left(\frac{D}{2}\right)^2F(\theta=\theta_m,\mathrm{EI},n) \tag{4.29}$$

Finally, solving for $w_{\perp,min}(m)$:

$$w_{\perp,min}(m)=\frac{D}{2}\left(\sqrt{F(\theta=\theta_m,\mathrm{EI},n)+1}-1\right) \tag{4.30}$$

Table 4.4 shows an example calculation of the minimum $w_\perp$ (as determined by PO trial and error) needed to cancel the first, second, and third sidelobe of a reflector having parameters in Table 4.3. Note that as $\mathbf{C}$ approaches continuous phase control, the observed minimum $w_\perp$ approaches $w_{\perp,min}$ calculated by Equation 4.30.

4.6 Summary

In summary, the procedure for estimating $w_{\perp,min}(m)$ for $m\leq 3$ or so, given only D, f/D, and either q or EI, is as follows:

Variable	Value
Frequency	1.5 GHz
f/D	0.40
D	90λ
q	1.14

Table 4.3: Parameters for the example in Section 4.5. Note that $q = 1.14$ corresponds to EI $= -11$ dB for a reflector with $D = 90\lambda$, where $\lambda = 0.2$ m.

		PO		
m	$w_{\perp,min}$	Cont. Phase	2-bit	1-bit
1	1.25λ	1.3λ	2λ	2.5λ
2	0.7λ	0.7λ	1λ	1.5λ
3	0.45λ	0.5λ	0.5λ	1λ

Table 4.4: $w_{\perp,min}$ calculated via Equation 4.30 compared to the result calculated using PO.

1. Using the procedure of Section 4.2, calculate either EI (if q is not known) or q (if EI is not known); then calculate n.

2. Using the method of Section 4.4, calculate θ_m.

3. Use Equation 4.30 to calculate $w_{\perp,min}(m)$.

In the case of continuous phase control, the actual value of $w_{\perp,min}$ calculated using PO is in good agreement with Equation 4.30, as expected. In the example presented in Section 4.5, the value of $w_{\perp,min}$ calculated using Equation 4.30 coarsely approximated the minimum value of $w_\perp$ for discrete phase control: In this case, Equation 4.30 underestimates this width, as expected.

Finally, note that Equation 4.30 is constrained to only produce a null in one direction. In general, a larger number of constraints requires more elements in an array. Extending this concept to the ERS, more constraints would presumably require a larger $w_\perp$ compared to the result calculated using Equation 4.30.

Chapter 5

Outrigger Panel Concept

In this chapter, we study four non-conformal ERS implementations. These four implementations consist of flat rectangular panels (i.e., "outrigger panels") attached to the rim of the non-reconfigurable portion of the reflector. Each design differs in the number of panels and their orientations along the rim of the non-reconfigurable portion of the reflector.

The organization of this chapter is as follows: In Section 5.1, the geometry of each outrigger panel configuration is defined. In Section 5.2, we provide the methodology for evaluating each outrigger panel configuration. In Sections 5.3-5.6, each outrigger panel configuration is evaluated.

5.1 Outrigger Panel Geometry and Orientation

Figure 5.1 shows an example outrigger panel system with rectangular panels having length, l, and panel width, w. The panels are attached to the rim of the non-reconfigurable portion of the reflector at the center of the panel's interior edge.

If there are p panels, then the length of each panel is ideally l_p (see Appendix A):

$$l_p = D \cot \frac{\pi(p-2)}{2p} \tag{5.1}$$

where $p \geq 3$ and D is the diameter of the non-reconfigurable portion of the reflector. However, l must be an integer multiple of the width of one ERS element, Δl. Thus, l can be set by rounding l_p down to the nearest integer multiple of Δl:

$$l \leftarrow \left\lfloor \frac{l_p}{\Delta l} \right\rfloor \cdot \Delta l \tag{5.2}$$

where $\lfloor \cdot \rfloor$ is the flooring function (see e.g., [16]). Note that this will create small gaps between each outrigger panel at the interior corners. The gaps are assumed to be small enough to not significantly affect the main lobe directivity or shape.

There are four outrigger panel configurations considered: Cases A, B, C, and D. These are summarized in Table 5.1. In Case A, the outrigger panels are attached tangent to the

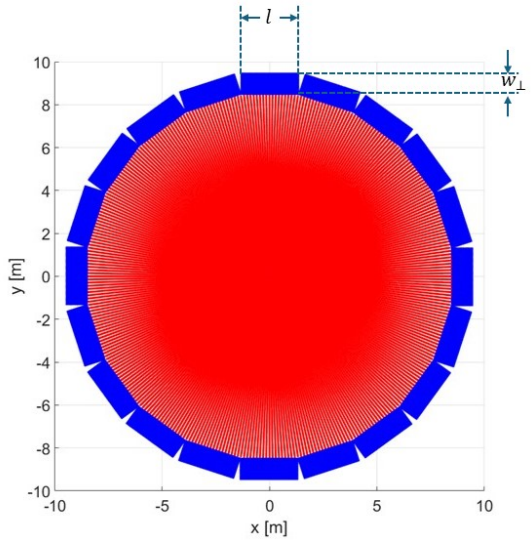

Figure 5.1: Example outrigger panel configuration consisting of p flat rectangular panels with dimensions $l \times w$. The *projected* area of each outrigger panel is $l \times w_\perp$.

rim of the non-reconfigurable portion of the reflector (see Figure 5.2). Case B is similar to Case A, but with every other outrigger panel removed (see Figure 5.8). The appeal of Case B is that fewer panels are used, reducing weight and cost. In Case C, the outrigger panels attached parallel to the aperture plane (see Figure 5.14). For the same $w_\perp$, Case C has a smaller w compared to Case A. This would reduce cost and weight of the panel, making Case C an attractive option. Case D is similar to Case C, but with every other panel removed (see Figure 5.20).

The conformal ERS implementation studied in the previous chapters will be referred to as Case 0. This serves as a baseline for comparison when assessing the performance of each outrigger panel configuration (see Sections 5.3–5.6).

Note that there are mechanical considerations to consider when physically realizing the outrigger panel systems, including flexing due to wind loading. If the panels are relatively long, then the effects from wind loading might alter the geometry significantly. If this is the case, we assume that there would be a higher cross-pol response due to the greater improper collimation of the electric field from the distortion of the geometry. Conversely, if the panels are relatively short, then we assume the effects to the antenna pattern to be negligible due to wind loading.

	Contiguous	Non-Contiguous
Tangent to the rim	Case A (Figure 5.2)	Case B (Figure 5.8)
Parallel to the aperture plane	Case C (Figure 5.14)	Case D (Figure 5.20)

Table 5.1: Outrigger configurations considered. "Contiguous" refers to outrigger panels placed contiguously and equidistant around the rim of the non-reconfigurable portion of the reflector (see e.g.,5.1). "Non-Contiguous" is akin to "Contiguous", but with every other outrigger panel removed.

5.2 Evaluation Methodology

Three scenarios are analyzed for each outrigger panel configuration: (1) When the ERS is in the quiescent state ("Quiescent" in Tables 5.4-5.7) where $C_n = 1 \ \forall \ n$, (2) When $\mathbf{C}$ is chosen to produce maximum directivity in the $+\hat{\mathbf{z}}$ direction ("Maximum" in Tables 5.4-5.7), and (3) When $\mathbf{C}$ is chosen to null in a particular direction ("Nulling" in Tables 5.4-5.7). The system design parameters are listed in Table 5.2. As in previous chapters, each ERS element is square with dimensions $\lambda/2 \times \lambda/2$. For all four cases, the nulling direction is $(\theta_m, \phi_m) = (1.75°, 0)$.

Using the design parameters listed in Table 5.2 with $p = 20$, $l_p \cong 14.25\lambda$, $l = 14\lambda$ m, the area of each outrigger panel is $l \times w \cong 84 \ \lambda^2$. These design parameters lead to 336 ERS elements for each outrigger panel. Note that the ratio of w:l is equal to 1:3.

Recall that $w_\perp$ is the projected width of the ERS. For the outrigger panels,

$$w_\perp(\psi) = w \ \sin\psi \tag{5.3}$$

where ψ is the tilt angle (see Equation B.6) of each outrigger panel with respect to the axis of symmetry of the reflector (see Figure B.1). Given the design parameters in Table 5.2, Equation B.6 yields $\psi \cong 58.00°$ for Cases A and B (see Appendix B). For Cases C and D, $\psi = 90°$.[1]

A useful quantity for assessing the performance is the aperture efficiency, ϵ_{ap}. Aperture efficiency is defined as the ratio of the effective aperture to the physical aperture. Instead of calculating the effective aperture directly, ϵ_{ap} can be calculated as the ratio of the main lobe directivity to that of a uniformly illuminated and perfectly co-polarized aperture of the same projected area:

$$\epsilon_{ap} = \frac{G}{G_{\text{UIA}}} \tag{5.4}$$

where:

$$G_{\text{UIA}} = \frac{4\pi}{\lambda^2} A \tag{5.5}$$

[1]Although not done in this thesis, making $w_\perp$ (Cases A & B) equal to $w_\perp$ (Case 0) would allow us to better compare Cases A to C, and Cases B to D. This is because the projected areas of Cases A and C would be the same, and the projected areas of Cases B and D would also be the same. This could be addressed in future work.

Variable	Value
Frequency	1.5 GHz
f/D	0.40
D	90λ
q	1.14
$w_\perp$ (Case 0)	6λ
w	6λ
$w_\perp$ (Cases A & B)	5.1λ
$w_\perp$ (Cases C & D)	6λ

Table 5.2: Design parameters for Case 0 and Cases A–D. Note that $q = 1.14$ leads to EI $= -11$ dB for a reflector with $D = 90\lambda$, where $\lambda = 0.2$ m.

	Case 0	Case A	Case B	Case C	Case D
A	326.85 m^2	311.46 m^2	282.96 m^2	321.67 m^2	288.07 m^2
υ	—	-4.7%	-13.4%	-1.6%	-11.9%

Table 5.3: Projected areas for Cases 0 and A–D given the design parameters in Table 5.2 and the percent difference, υ, of the projected areas for Cases A–D compared to Case 0.

and A is the projected area of the aperture. For Case 0, the aperture is circular with diameter equal to $D + 2w_\perp$, so

$$A = \pi \left(\frac{D + 2w_\perp}{2} \right)^2 \tag{5.6}$$

For Cases A–D, we can calculate A by summing the projected area of the non-reconfigurable portion of the reflector, A_0:

$$A_0 = \pi \left(\frac{D}{2} \right)^2 \tag{5.7}$$

and p times the projected area of one outrigger panel, A_r:

$$A_r = w_\perp \, l \tag{5.8}$$

The projected areas for Cases 0 and A–D are listed in Table 5.3.

Note that there is diffraction associated with the edges of each outrigger panel. For this thesis, diffraction effects were not considered, and they might have an effect on the pattern near the main lobe. This would be the topic of future work.

	Quiescent		Maximum	Nulling	
	Case 0	Case A	Case A	Case 0	Case A
G	48.89 dBi	48.18 dBi	48.68 dBi	48.20 dBi	48.20 dBi
ΔG	–	−0.71 dB	−0.21 dB	−0.69 dB	−0.69 dB
	–	−15.1 %	−4.7 %	−14.7 %	−14.7 %
ϵ_{ap}	0.76	0.67	0.76	0.64	0.67
HPBW	0.80°	0.80°	0.79°	0.78°	0.80°
SLL	27.61 dB	27.42 dB	26.00 dB	27.01 dB	26.53 dB
Peak XPOL	–	−35.00 dBi	−35.50 dBi	−12.56 dBi	−21.20 dBi
Null Depth	–	–	–	−70.50 dBi	−65.26 dBi

Table 5.4: Results for Case A and comparison to Case 0. Note that ΔG is ratio of gain compared to Case 0 Quiescent. Note that "XPOL" is cross-pol, and the "Null Depth" is the directivity in the direction of the desired null.

5.3 Case A (Contiguous and Tangent)

A front and side view of Case A is shown in Figure 5.2. The aperture efficiency (ϵ_{ap}), main lobe directivity (G), HPBW, and SLL for all three scenarios are listed in Table 5.4. Also listed in the table is the peak cross-pol for each scenario, as well as the depth of the null in the desired direction.

Quiescent: Figure 5.3 shows the co-pol and cross-pol directivity patterns, and Figure 5.4 shows the H-plane patterns. Compared to Case 0, Case A has a 15.1% lower main lobe directivity. Since the projected area of Case A is 4.7% smaller than Case 0's, the improper collimation must account for the 11.4% lower main lobe directivity.

Maximum: The co-pol and cross-pol directivity patterns are shown in Figure 5.5 and the H-plane patterns are shown in Figure 5.4. Compared to Case 0, the main lobe directivity of Case A is approximately 4.7% lower. Thus, when the ERS is set to maximize the main lobe directivity, the gain lost through improper collimation can be nearly eliminated.

Nulling: The co-pol and cross-pol directivity patterns are shown in Figure 5.6 and the H-plane patterns are shown in Figure 5.7. Case A produces a null depth of −65.26 dBi in the direction of the desired null. Compared to Case 0, Case A achieves nulling without any significant decrease in the main lobe directivity, HPBW, and SLL compared to Case 0. Additionally, Case A exhibits a 5.24 dB lower peak cross-pol than Case 0. This is unexpected, as the SSA did not optimize the cross-pol for Case A.

5.4 Case B (Non-Contiguous and Tangent)

A front and side view of Case B is shown in Figure 5.8. The aperture efficiency, main lobe directivity, HPBW, and SLL for all three scenarios are listed in Table 5.5. Also listed in the table is the peak cross-pol for each scenario, as well as the depth of the null in the desired

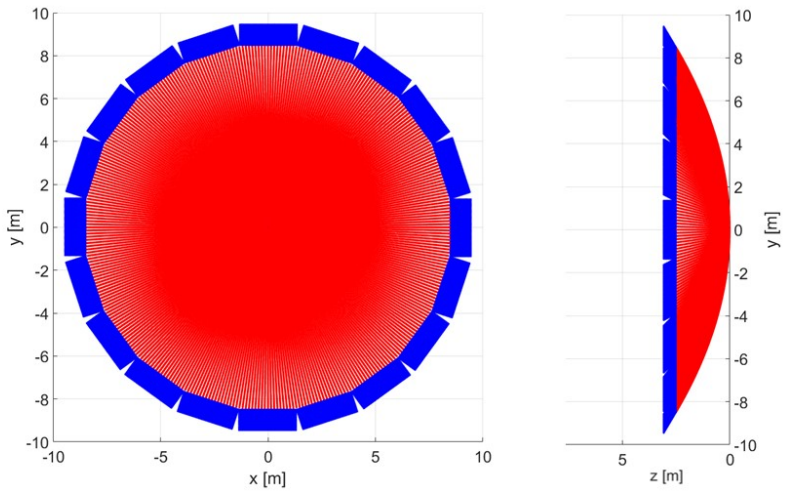

Figure 5.2: Front and side views of Case A with 20 outrigger panels and design parameters given in Table 5.2.

direction.

Quiescent: The co-pol and cross-pol directivity patterns are shown in Figure 5.9 and Figure 5.10 shows the H-plane patterns. Compared to Case 0, Case B has a 16.6% lower main lobe directivity. Since the projected area of Case B is 13.4% lower than in Case 0, the improper collimation must account for the 3.2% lower main lobe directivity.

Maximum: The co-pol and cross-pol directivity patterns are shown in Figure 5.11 and Figure 5.10 shows the H-plane patterns. Compared to Case 0, the main lobe directivity of Case B is 13.5% lower. Similar to Case A, the ERS nearly eliminates the gain lost due to improper collimation for Case B. However, note that the ERS cannot recover the gain lost due to the smaller aperture compared to Cases A and 0.

Nulling: The co-pol and cross-pol directivity patterns are shown in Figure 5.12 and Figure 5.13 shows the H-plane patterns. Case B produces a null depth equal to -58.02 dBi in the desired direction, and a 25.64 dB and 17.00 dB lower peak cross-pol compared to Cases 0 and A, respectively. The lower cross-pol is due to Case A being able to contribute more to the cross-pol than Case B since there are double the number of panels. If cross-pol performance is an issue, then Case B is preferable to Case A. However, Case A provides a 6.24 dB deeper null depth than Case B. This is because Case A has more panels than Case B, which allows the ERS to reflect more energy to produce a deeper null.

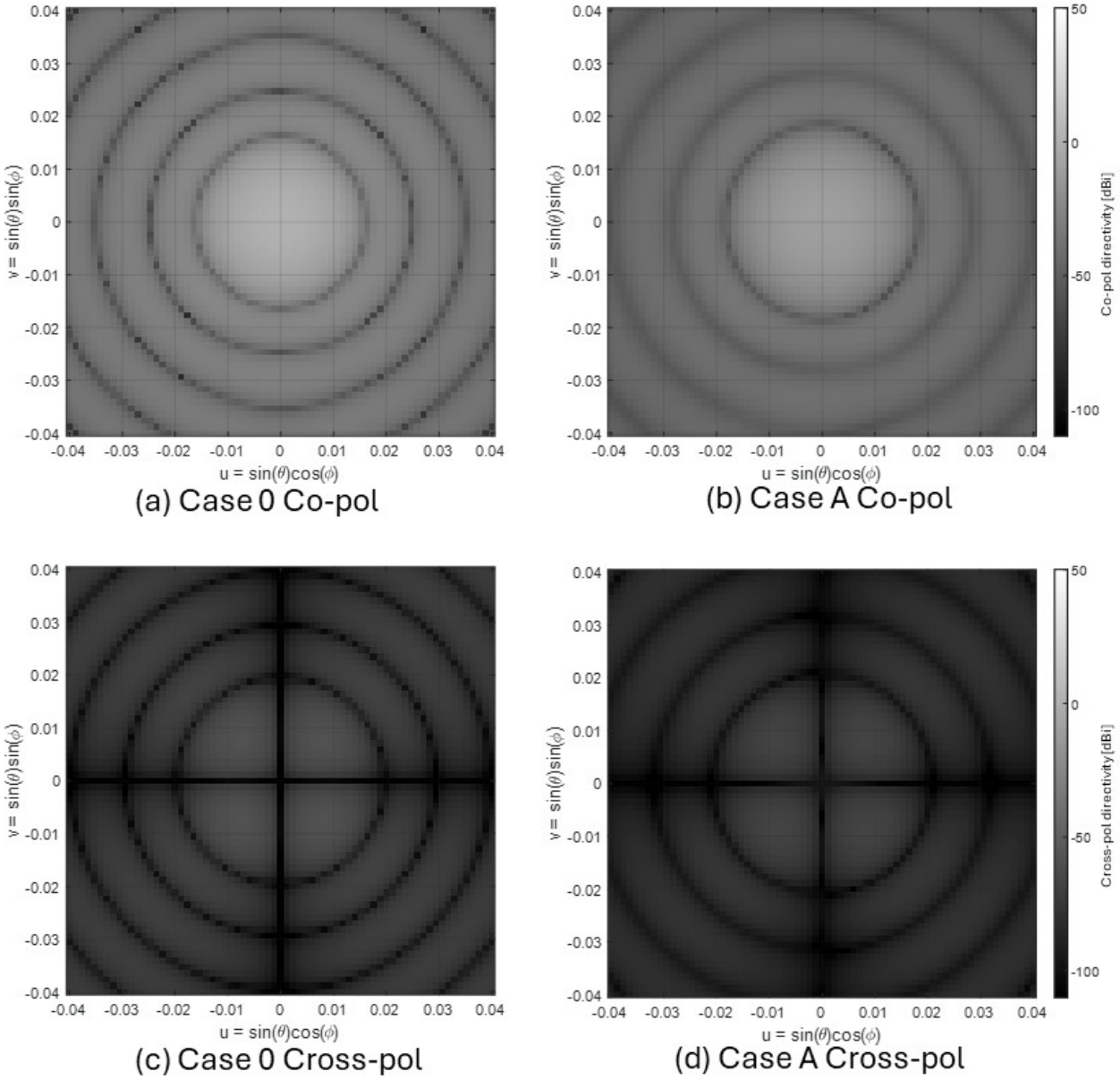

Figure 5.3: Case 0 and Case A, Quiescent state.

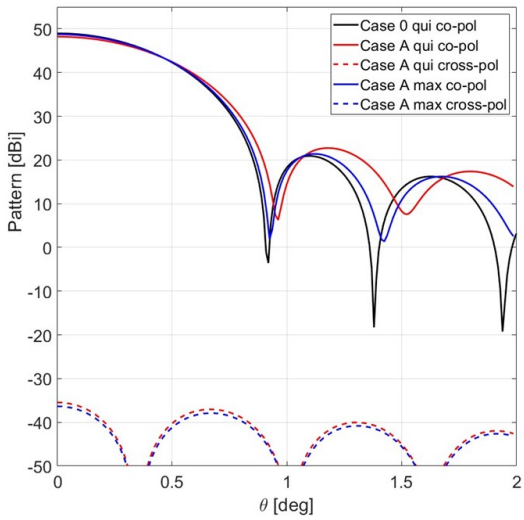

Figure 5.4: H-plane directivity for Case 0 and Case A for the Maximum state and Quiescent state.

	Quiescent		Maximum	Nulling	
	Case 0	Case B	Case B	Case 0	Case B
G	48.89 dBi	48.10 dBi	48.26 dBi	48.20 dBi	48.12 dBi
ΔG	–	−0.79 dB	−0.63 dB	−0.69 dB	−0.77 dB
	–	−16.6 %	−13.5 %	−14.7 %	−16.3 %
ϵ_{ap}	0.76	0.74	0.79	0.64	0.74
HPBW	0.80°	0.80°	0.80°	0.78°	0.78°
SLL	27.61 dB	25.60 dB	26.03 dB	27.01 dB	27.05 dB
Peak XPOL	–	−42.03 dBi	−43.00 dBi	−12.56 dBi	−38.20 dBi
Null Depth	–	–	–	−70.50 dBi	−58.02 dBi

Table 5.5: Results for Case B and comparison to Case 0. Note that ΔG is ratio of gain compared to Case 0 Quiescent. Note that "XPOL" is cross-pol, and the "Null Depth" is the directivity in the direction of the desired null.

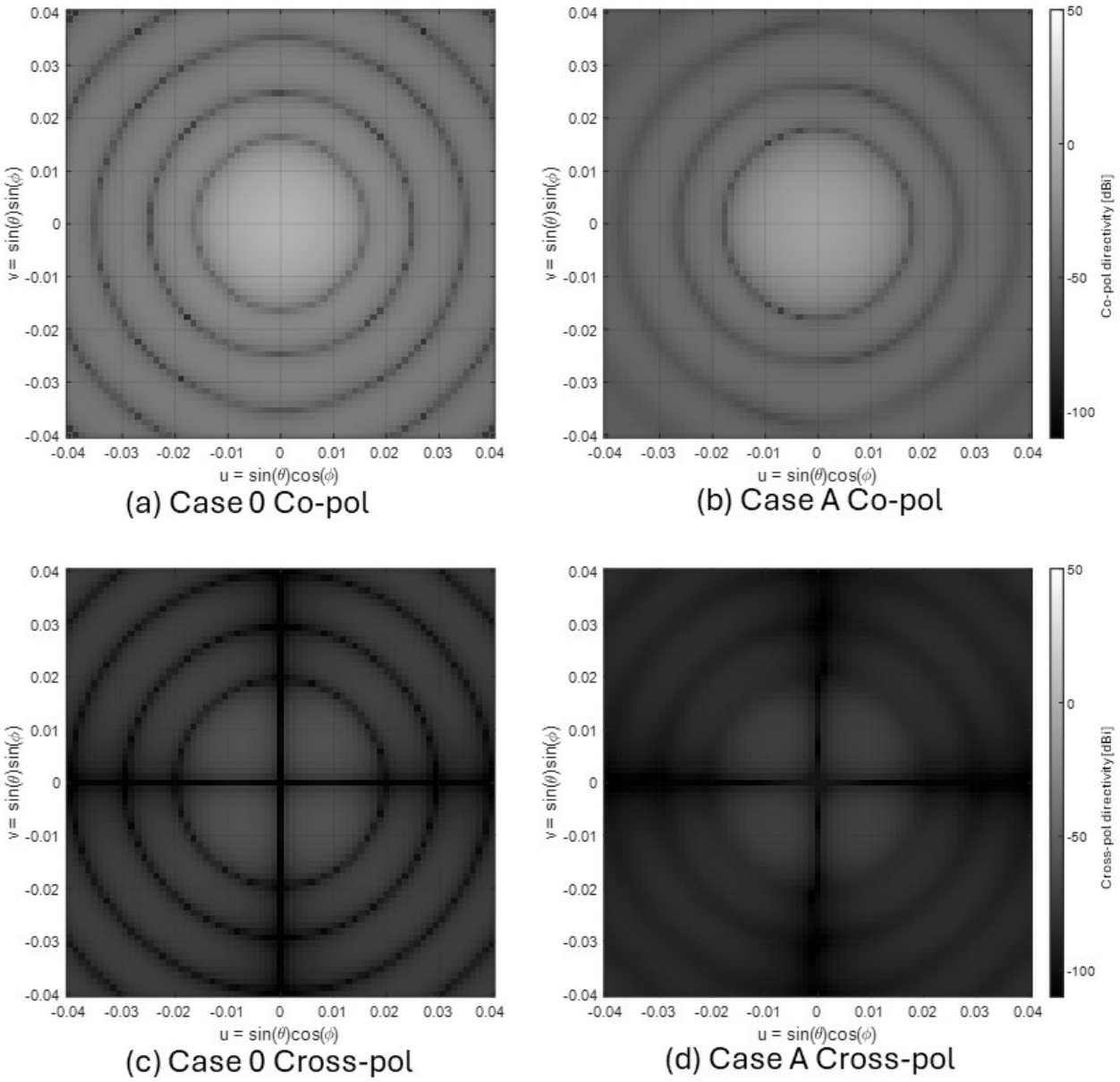

Figure 5.5: Case 0 and Case A, Maximum State.

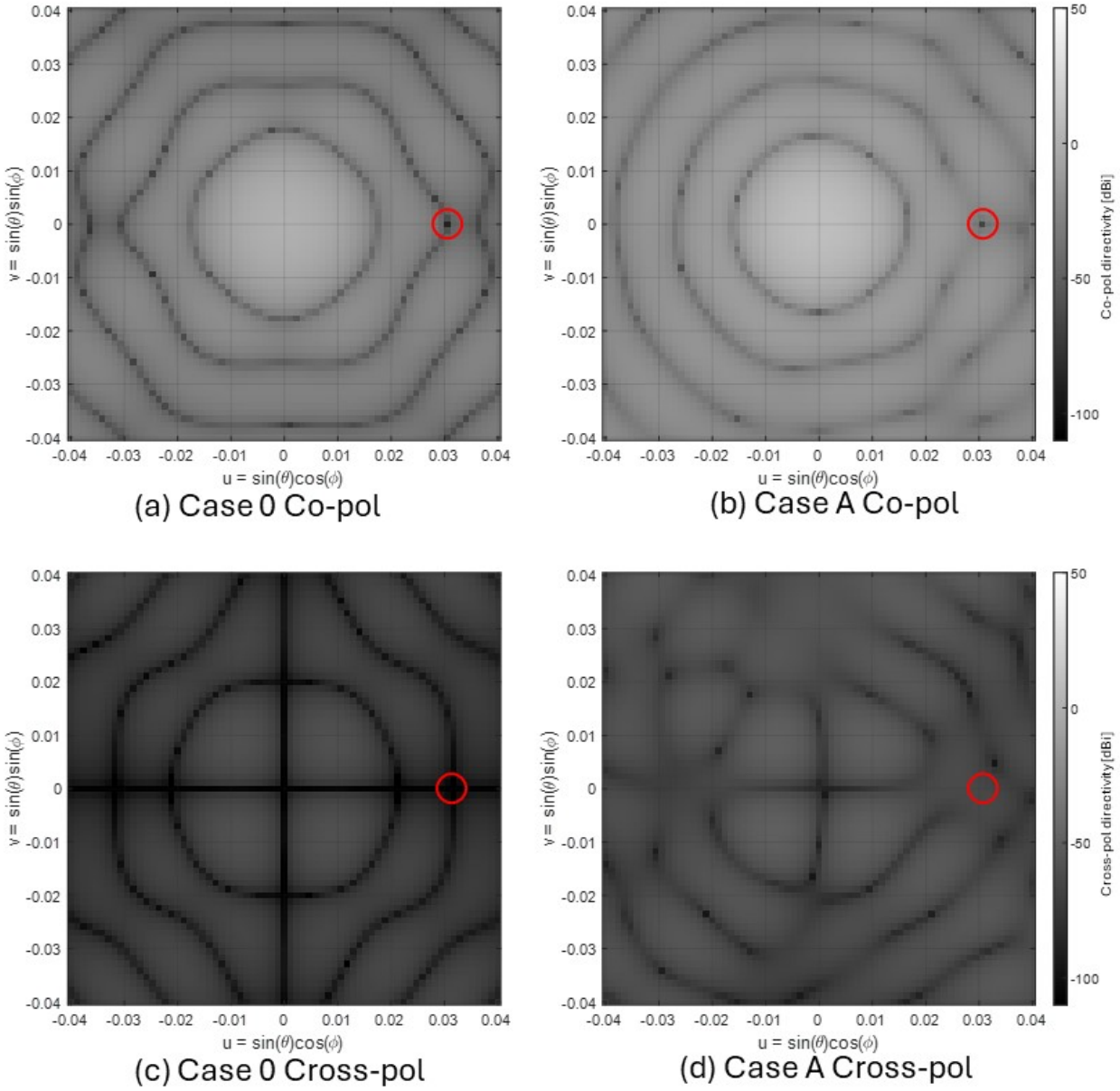

Figure 5.6: Case 0 and Case A, nulling state. The red circle indicates the location of the null.

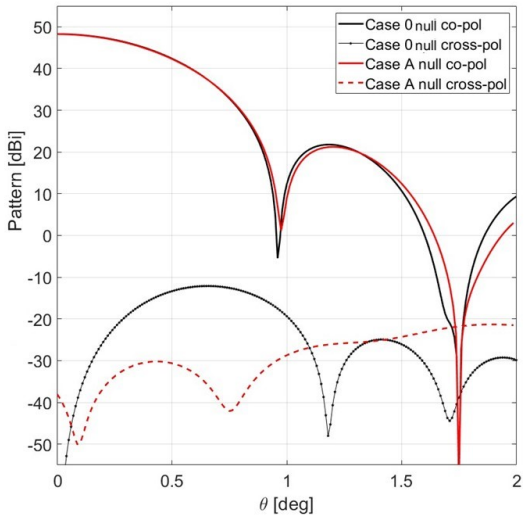

Figure 5.7: H-plane result for Case A and Case 0 in the nulling state.

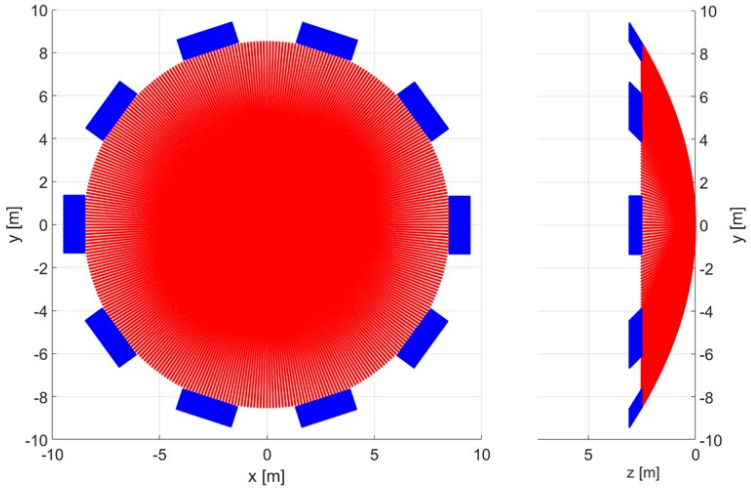

Figure 5.8: Front and side views of Case B with 10 outrigger panels and design parameters given in Table 5.2.

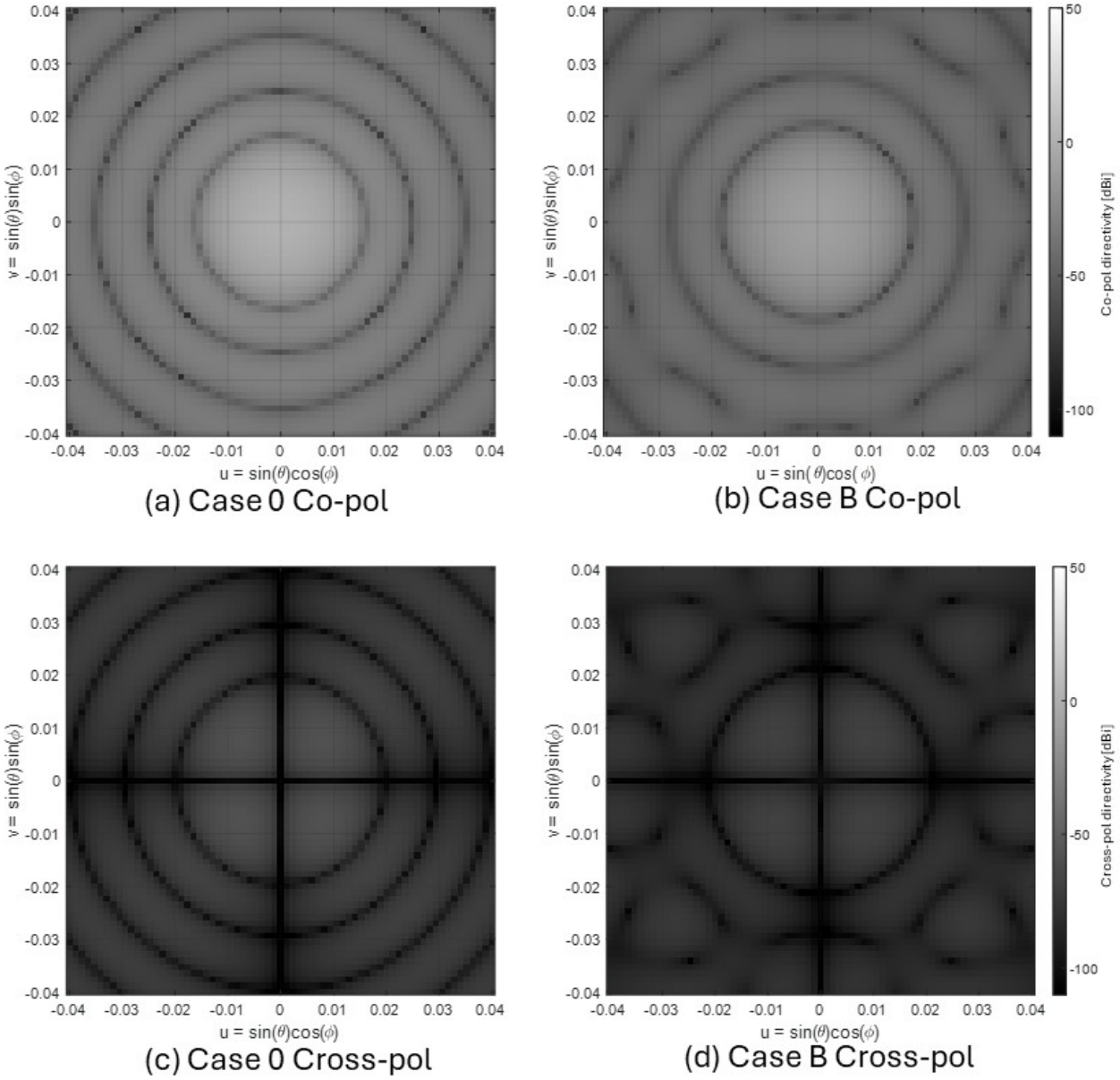

Figure 5.9: Case 0 and Case B, Quiescent State.

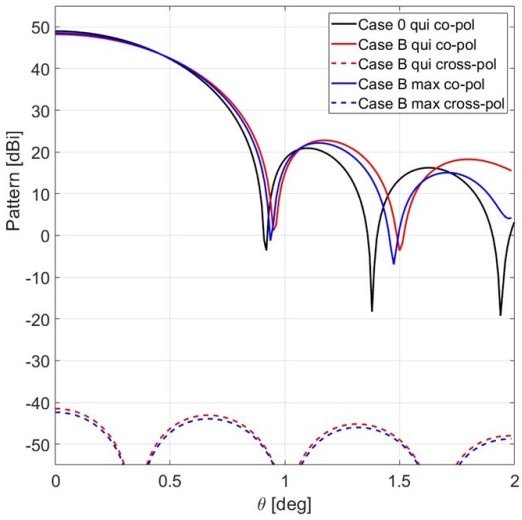

Figure 5.10: H-plane result for Case B and Case 0 for the Maximum State and Quiescent State.

5.5 Case C (Contiguous and Non-Tangent)

A front and side view of Case C is shown in Figure 5.14. The aperture efficiencies, main lobe directivity, HPBW, and SLL for all three scenarios are listed in Table 5.6. Also listed in the table is the peak cross-pol for each scenario, as well as the depth of the null in the desired direction.

Quiescent: The co-pol and cross-pol directivity patterns are shown in Figure 5.15 and the H-plane patterns are shown in Figure 5.16. Compared to Case 0, Case C has a 14.5% lower main lobe directivity. Since the projected area is 1.6% smaller than Case 0's, the improper collimation must account for the 12.9% lower main lobe directivity.

Maximum: The co-pol and cross-pol directivity patterns are shown in Figure 5.17 and the H-plane patterns are shown in Figure 5.16. Compared to Case 0, the main lobe directivity in Case C is 6.2% lower. This indicates that no amount of optimization allows Case C to eliminate the gain lost through improper collimation. We conclude that the collimation for Case C is worse than Cases A and B.

Nulling: The co-pol and cross-pol directivity patterns are shown in Figure 5.18 and the H-plane result is shown in Figure 5.19. Case C produces a null depth of -33.20 dBi in the desired direction. The peak cross-pol for Case C is 26.22 dB and 43.22 dB higher compared to Cases A and B, respectively. The higher cross-pol is expected as Case C has a worse collimation compared to Cases A and B.

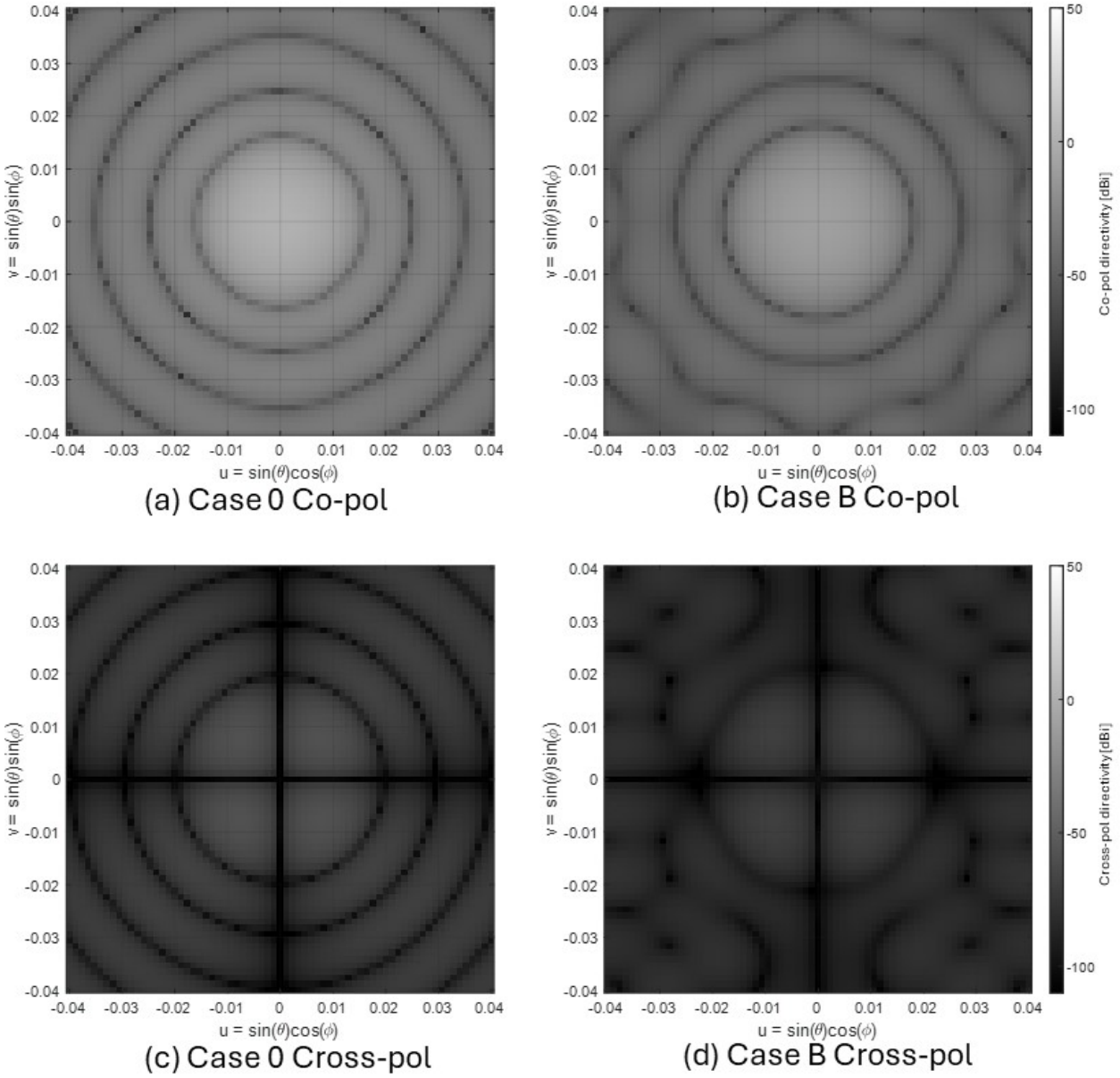

Figure 5.11: Case 0 and Case B, Maximum State.

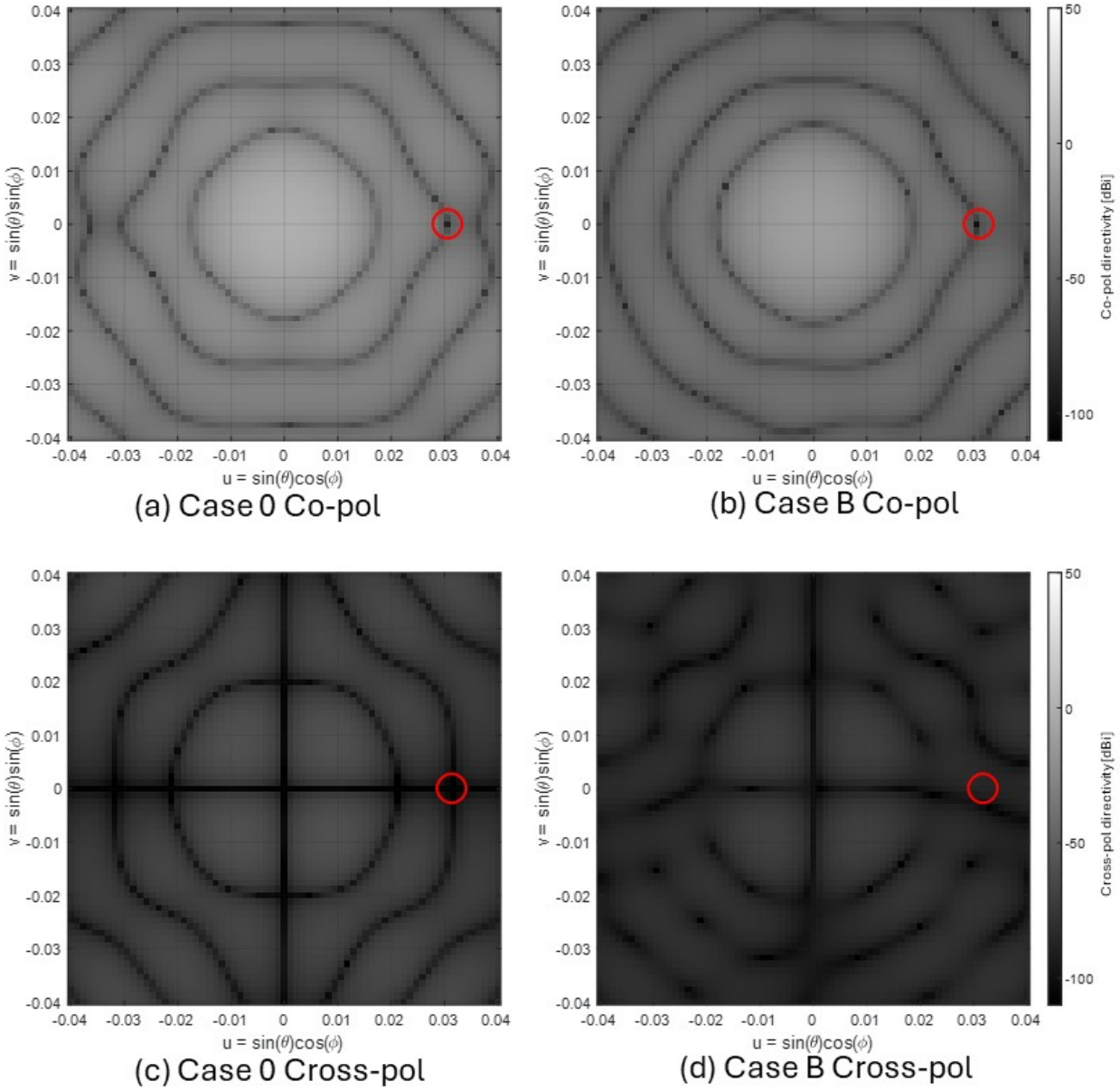

Figure 5.12: Case 0 and Case B, nulling state. The red circle indicates the location of the null.

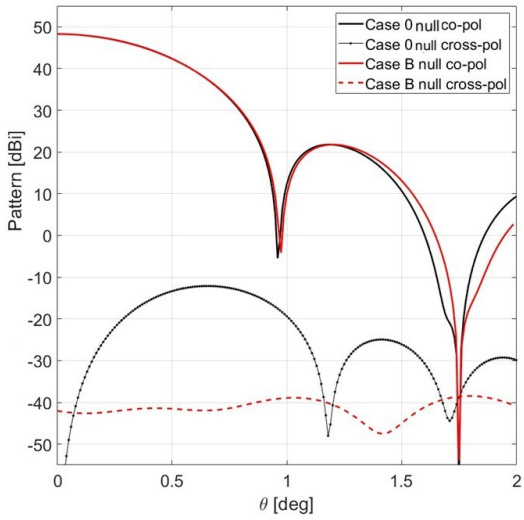

Figure 5.13: H-plane result for Case B and Case 0 in the nulling state.

	Quiescent		Maximum	Nulling	
	Case 0	Case C	Case C	Case 0	Case C
G	48.89 dBi	48.21 dBi	48.61 dBi	48.20 dBi	48.30 dBi
ΔG	–	−0.78 dB	−0.28 dB	−0.69 dB	−0.59 dB
	–	−14.5 %	−6.2 %	−14.7 %	−12.7 %
ϵ_{ap}	0.76	0.65	0.72	0.64	0.67
HPBW	0.80°	0.80°	0.80°	0.78°	0.65°
SLL	27.61 dB	25.31 dB	26.03 dB	27.01 dB	26.52 dB
Peak XPOL	–	−35.70 dBi	−75.00 dBi	−12.56 dBi	5.02 dBi
Null Depth	–	–	–	−70.50 dBi	−33.20 dBi

Table 5.6: Results for Case C and comparison to Case 0. Note that ΔG is ratio of gain compared to Case 0 Quiescent. Note that "XPOL" is cross-pol, and the "Null Depth" is the directivity in the direction of the desired null.

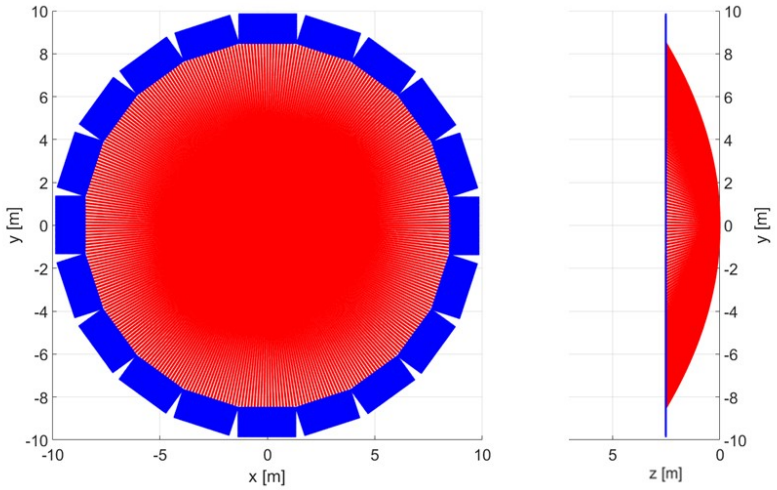

Figure 5.14: Front and side views of Case C with 20 outrigger panels and specifications given in Table 5.2.

5.6 Case D (Non-Contiguous and Non-Tangent)

A front and side view of Case D is shown in Figure 5.20. The aperture efficiency, main lobe directivity, HPBW, and SLL for all three scenarios are listed in Table 5.7. Also listed in the table is the peak cross-pol for each scenario, as well as the depth of the null in the desired direction.

Quiescent: The co-pol and cross-pol directivity patterns are shown in Figure 5.21 and the H-plane pattern is shown in Figure 5.22. Compared to Case 0, Case D has a 14.7% lower main lobe directivity. Since the projected area of Case D is 11.9% lower than in Case 0, the improper collimation must account for the 3.1% lower main lobe directivity.

Maximum: The co-pol and cross-pol directivity patterns are shown in Figure 5.23 and the H-plane pattern is shown in Figure 5.22. Compared to Case 0, the main lobe directivity is 12.7% lower for Case D. We conclude that Case D is unable to recover the gain lost through improper collimation. Note that Case D produces a very low (−80.02 dBi) peak cross-pol, similar to Case C.

Nulling: The co-pol and cross-pol directivity patterns are shown in Figure 5.24. Figure 5.25 shows the H-plane patterns for Cases 0 and D. Case D produces a null depth of −29.70 dBi. The peak cross-pol for Case D is 18.06 dB lower than Case C in the nulling state. The reasoning behind the higher peak cross-pol in Case C compared to Case D is due to the extra panels of the former contributing more to the cross-pol. Thus, it is unsurprising that

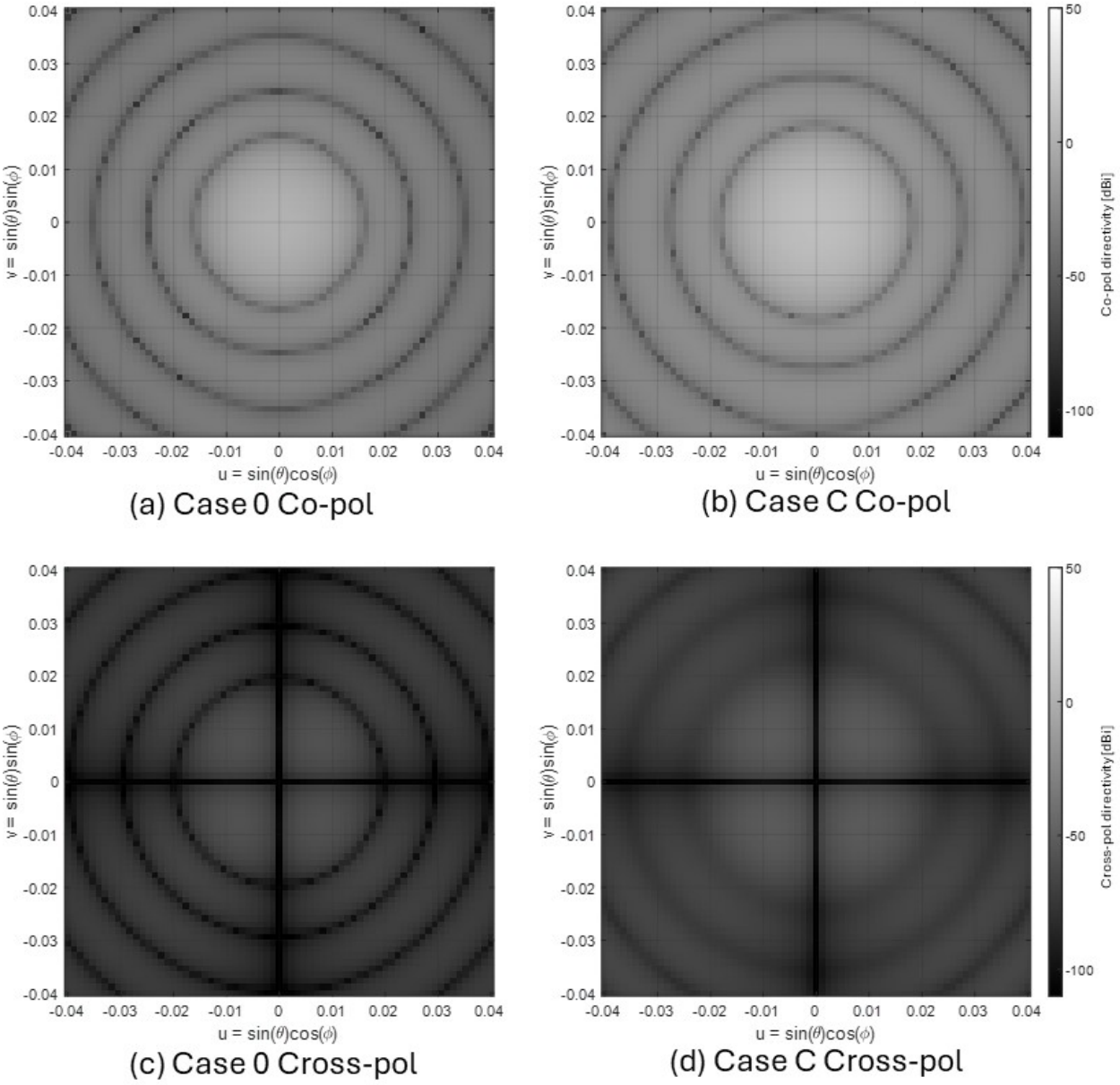

Figure 5.15: Case 0 and Case C, Quiescent State.

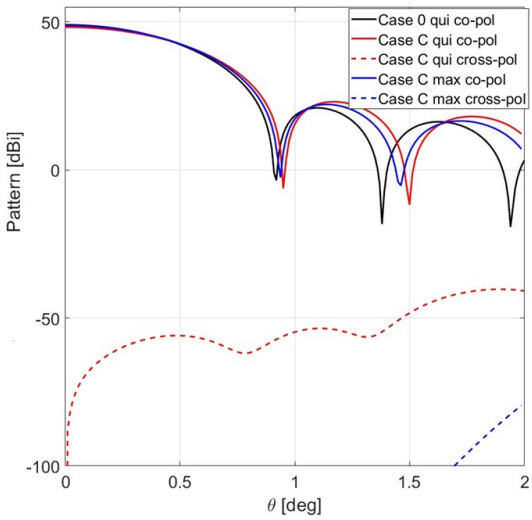

Figure 5.16: H-plane result for Case C and Case 0 in the Maximum State and Quiescent State.

	Quiescent		Maximum	Nulling	
	Case 0	Case D	Case D	Case 0	Case D
G	48.89 dBi	48.20 dBi	48.30 dBi	48.20 dBi	48.22 dBi
ΔG	–	−0.69 dB	−0.59 dB	−0.69 dB	−0.67 dB
	–	−14.7 %	−12.7 %	−14.7 %	−14.3 %
ϵ_{ap}	0.76	0.73	0.76	0.64	0.75
HPBW	0.80°	0.80°	0.79°	0.78°	0.80°
SLL	27.61 dB	25.52 dB	27.50 dB	27.01 dB	27.04 dB
Peak XPOL	–	−59.88 dBi	−80.02 dBi	−12.56 dBi	−31.02 dBi
Null Depth	–	–	–	−70.50 dBi	−70.20 dBi

Table 5.7: Results for Case D and comparison to Case 0. Note that ΔG is ratio of gain compared to Case 0 Quiescent. Note that "XPOL" is cross-pol, and the "Null Depth" is the directivity in the direction of the desired null.

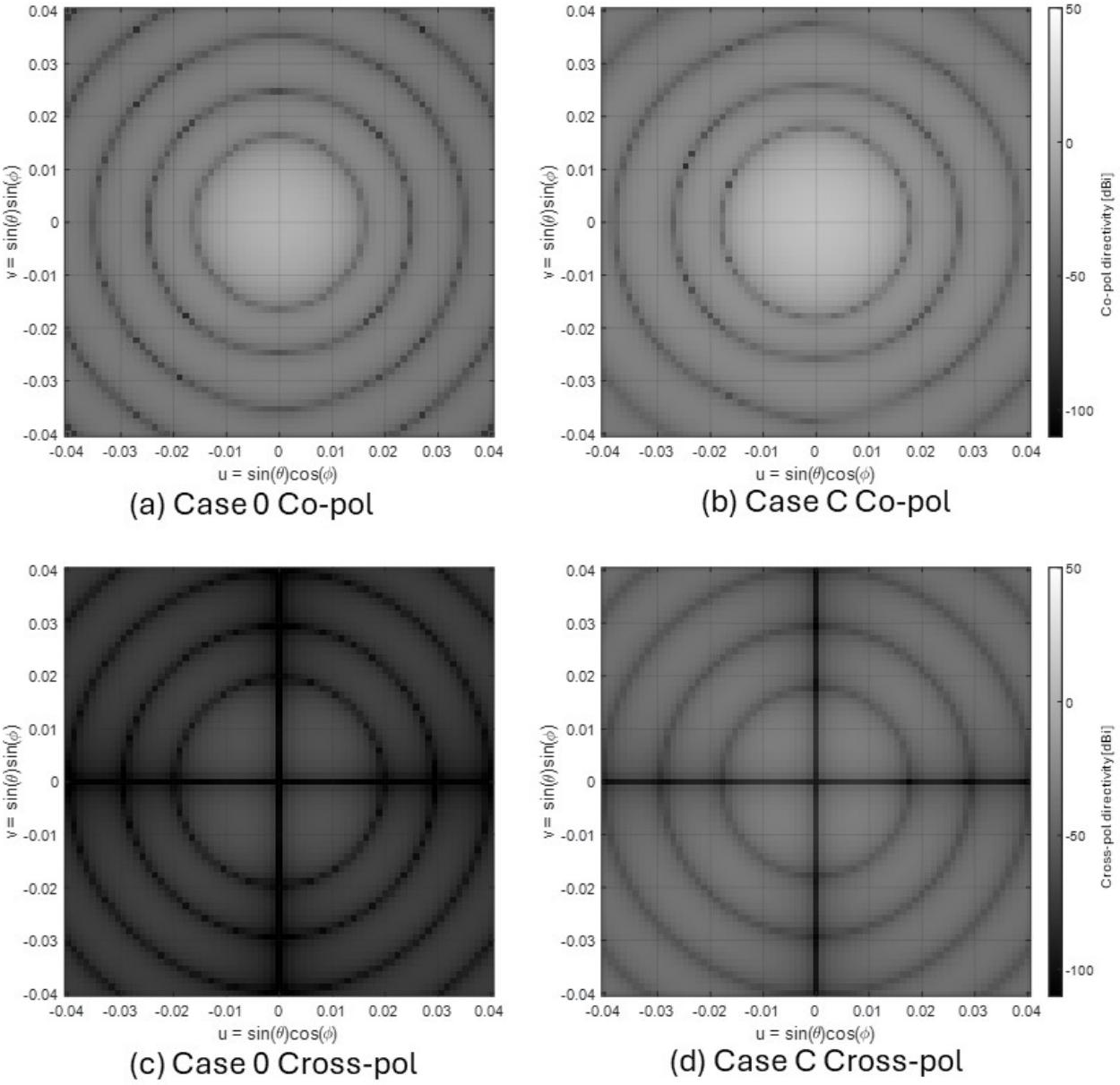

Figure 5.17: Case 0 and Case C, Maximum State.

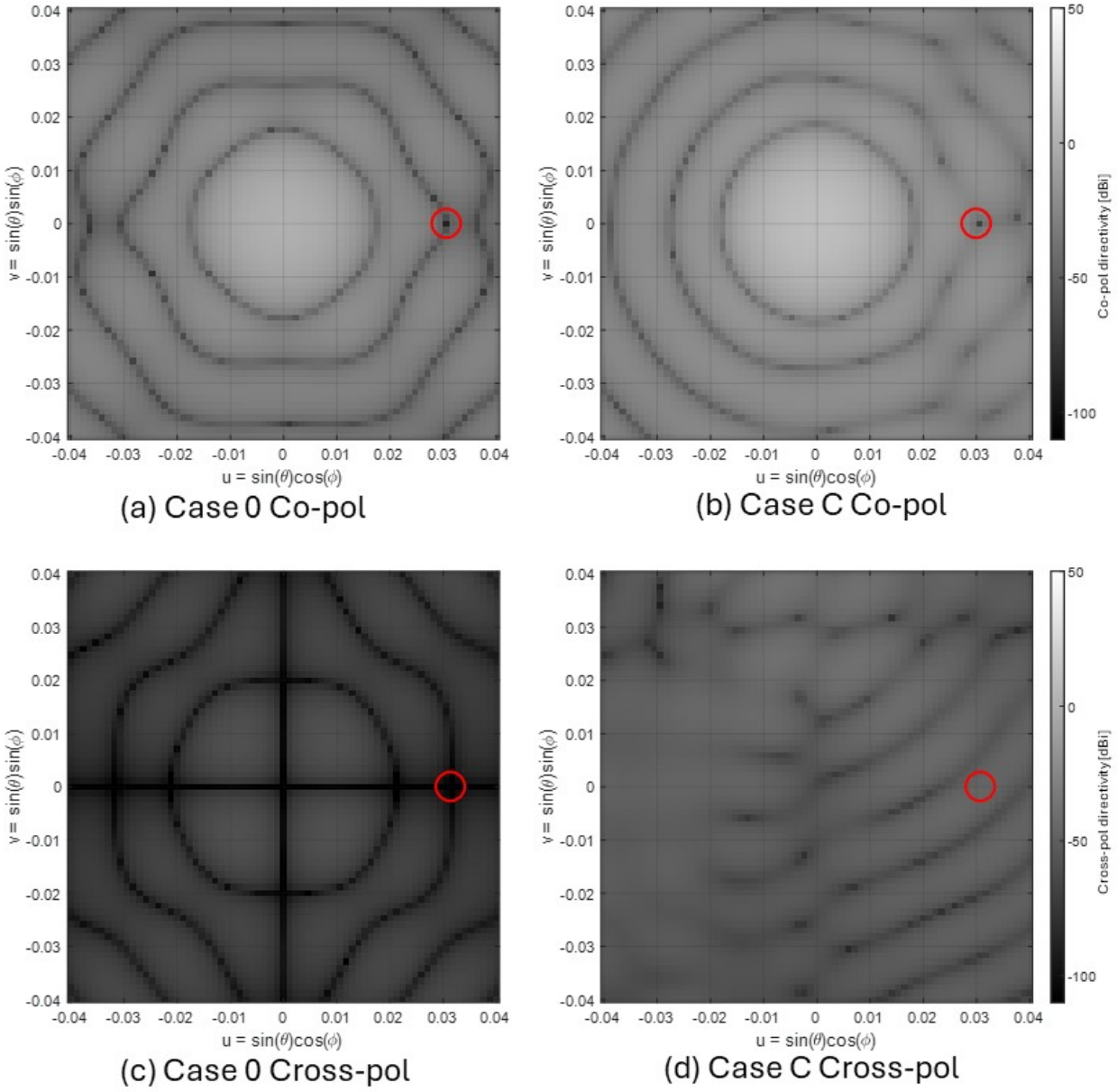

Figure 5.18: Case 0 and Case C, nulling state. The red circle indicates the location of the null.

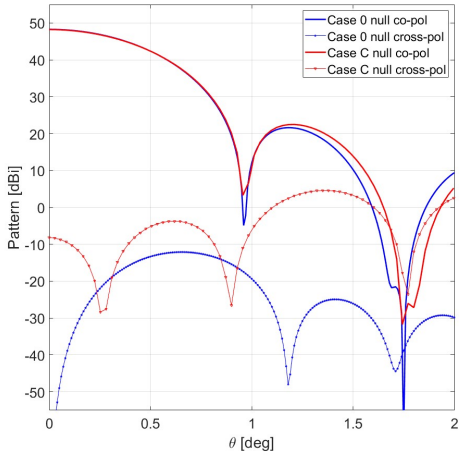

Figure 5.19: H-plane result for Case C and Case 0 for the nulling state.

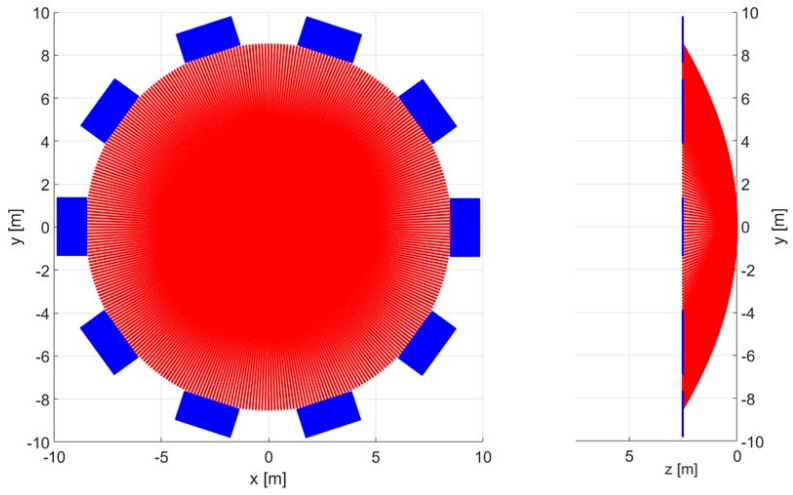

Figure 5.20: Front and side views of Case D with 10 outrigger panels and specifications given in Table 5.2.

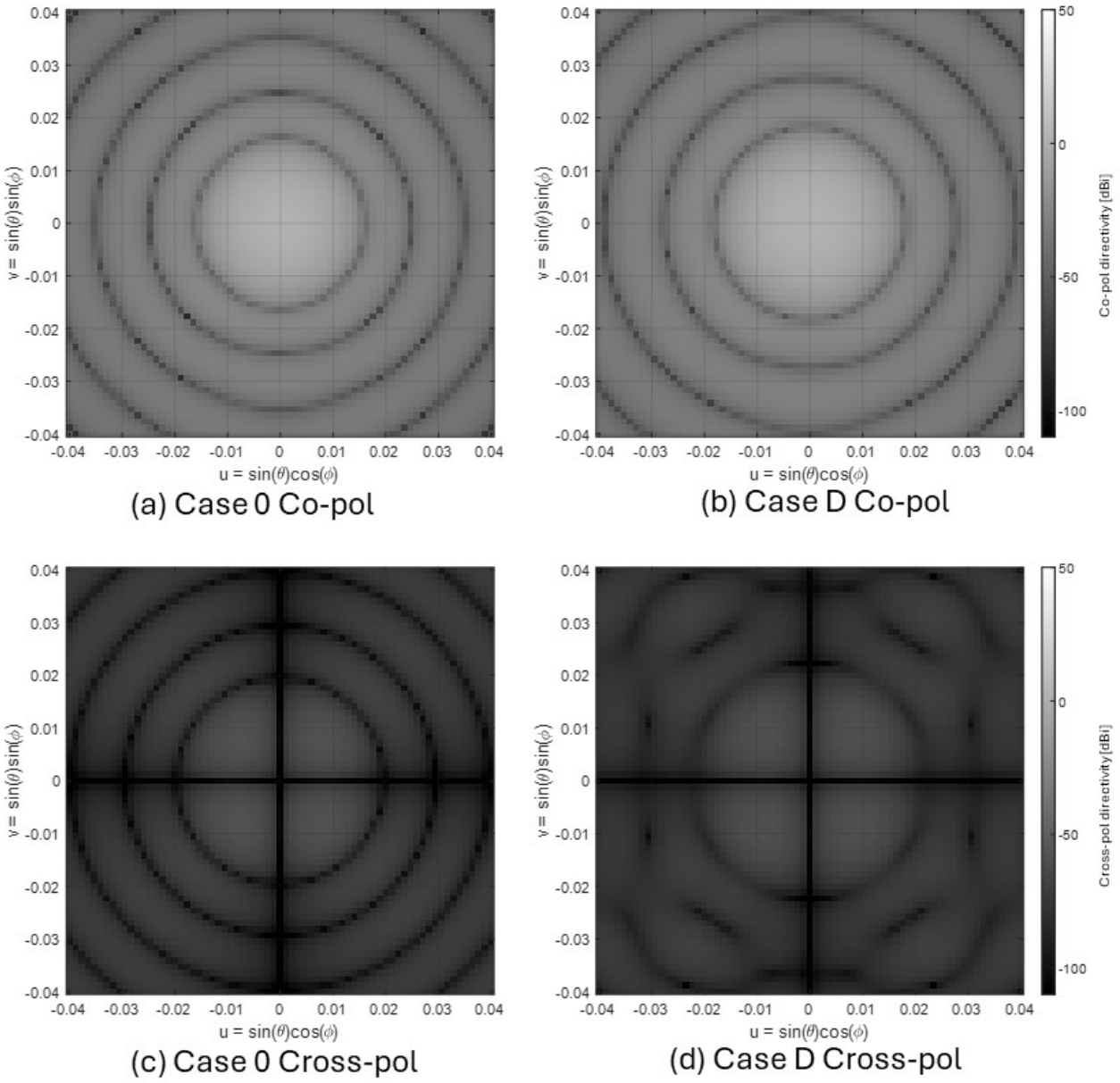

Figure 5.21: Case 0 and Case D, Quiescent State.

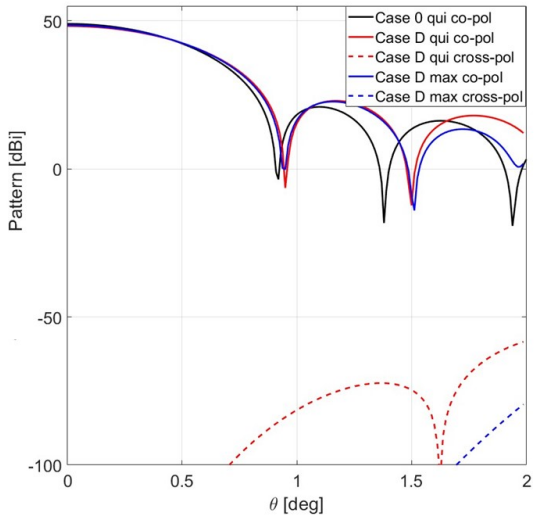

Figure 5.22: H-plane result for Case D and Case 0 for the Quiescent and Maximum States.

the peak cross-pol for Case C is higher than Case D.

5.7 Conclusions

Table 5.8 provides a comparison of key performance quantities for Cases 0 and A-D. All four outrigger panel configurations demonstrate that a null can be produced in the desired direction. We conclude that all the outrigger panel configurations considered in this thesis are suitable alternatives for the conformal ERS implementation.

For the outrigger panel configurations, the peak cross-pol in the nulling state for Case C is the highest, followed by Cases A, D, and B. Thus, if the best cross-pol performance is required, Case B is desirable. However, Case B exhibits the lowest main lobe directivity in the nulling state. If the peak cross-pol is a non-issue, and a higher main lobe directivity is desired, then Case C is the best option, followed by Cases D, A, and B. Lastly, if the deepest null depth is required, then Case D would be the best option, followed by Cases A, B, and C.

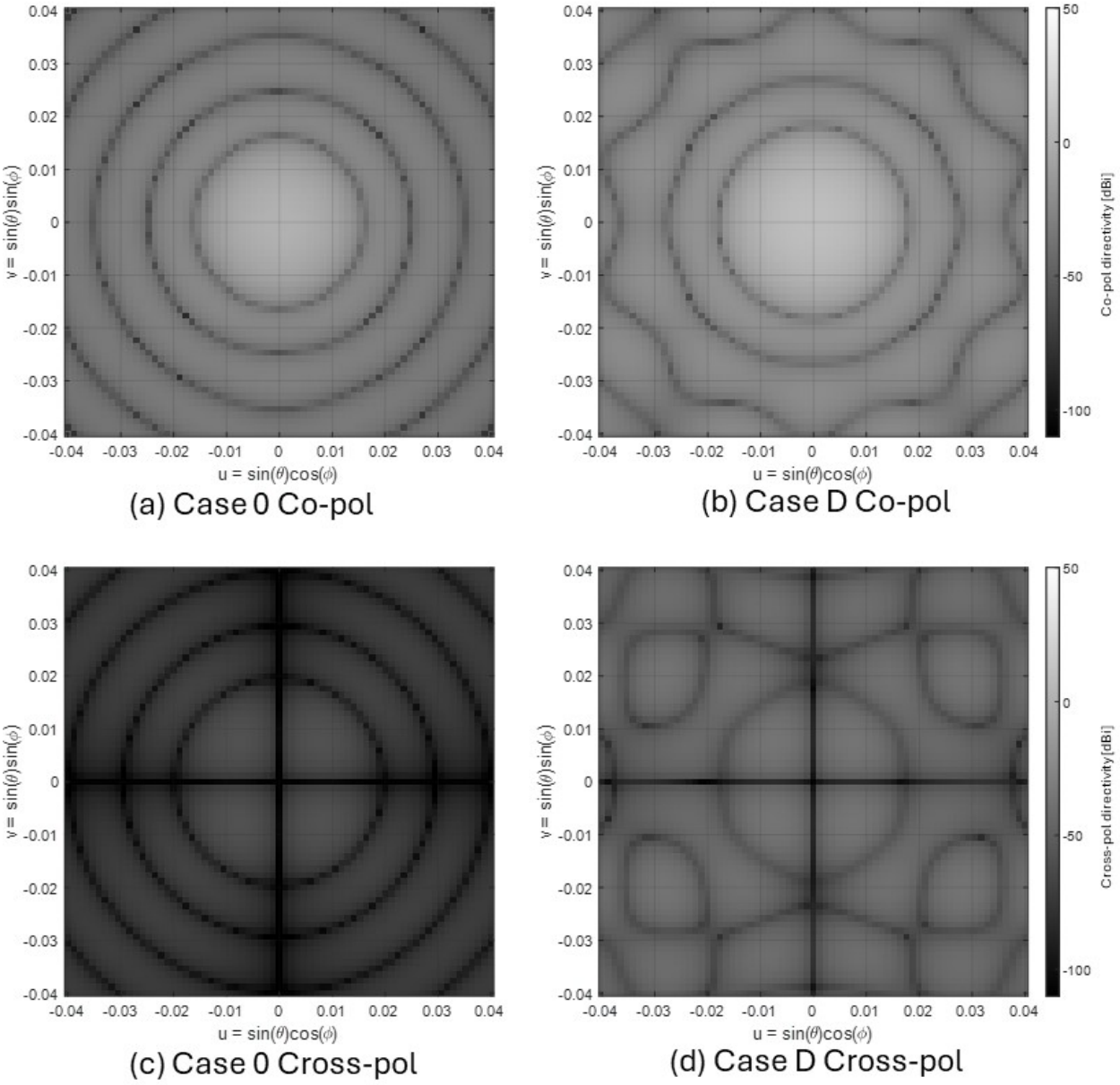

Figure 5.23: Case 0 and Case D, Maximum State.

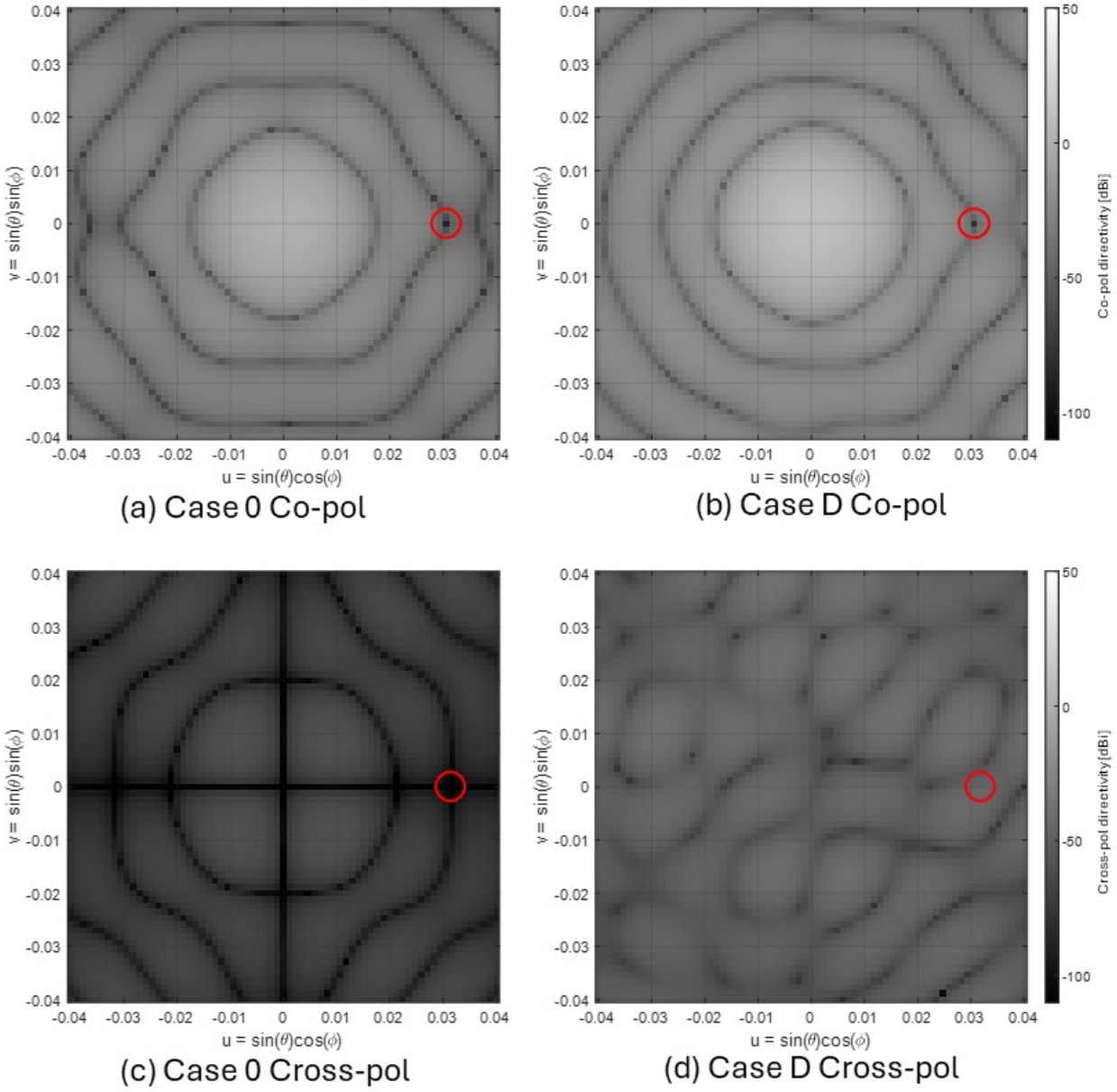

Figure 5.24: Case 0 and Case D, nulling state. The red circle indicates the location of the null.

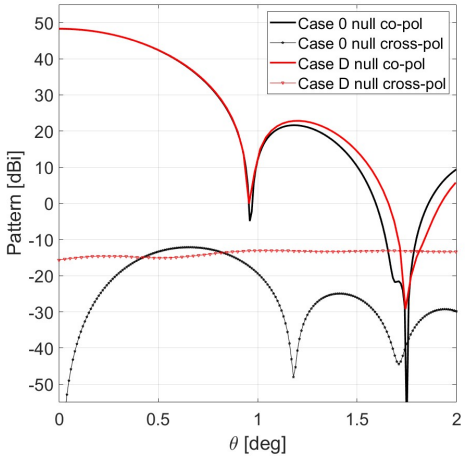

Figure 5.25: H-plane result for Case D and Case 0 in the nulling state.

	Case 0	Case A	Case B	Case C	Case D
G(Quiescent)	48.89 dBi	48.18 dBi	48.10 dBi	48.21 dBi	48.20 dBi
G(Maximum)	48.89 dBi	48.68 dBi	48.26 dBi	48.61 dBi	48.30 dBi
G(Nulling)	48.20 dBi	48.20 dBi	48.12 dBi	48.30 dBi	48.31 dBi
Peak XPOL(Quiescent)	–	−35.00 dBi	−42.03 dBi	−35.70 dBi	−59.88 dBi
Peak XPOL(Maximum)	–	−35.50 dBi	−43.00 dBi	−75.00 dBi	−80.02 dBi
Peak XPOL(Nulling)	−12.56 dBi	−21.20 dBi	−38.20 dBi	5.02 dBi	−13.04 dBi
Null Depth	−70.50 dBi	−65.26 dBi	−58.02 dBi	−33.20 dBi	−29.70 dBi

Table 5.8: Key values for the null depth and peak cross-pol values for Cases A-D. Note "XPOL" is equivalent to cross-pol, and the "Null Depth" applies to the nulling state exclusively.

Chapter 6

Conclusions and Work Path Forward

6.1 Summary of Contributions

The contributions of this thesis are summarized below:

- For the conformal ERS implementation, an approximate, closed form expression for the minimum rim width of the ERS to null the m^{th} sidelobe is developed in Section 4.5. The final result given by Equation 4.30. This equation is validated via an example where the results are compared to these calculated using PO. This comparison is shown in Table 4.4.
- The designs of four outrigger panel configurations are presented in Section 5.1. We discussed the efficacy of nulling. as well as other performance characteristics in Sections 5.3-5.6, with the results are summarized in Table 5.8. For the given design parameters in Table 5.2, it was concluded that Cases C and D could not recover the gain lost through improper collimation and created a shallower null compared to Cases A and B. Additionally, Cases C and D exhibited a higher peak cross-pol and lower null depths compared to Cases A and B.

6.2 Future Work

Suggested future work includes:

- Performing a study on the efficacy of nulling by attaching the outrigger panels on dual reflector and offset reflector antennas. Dual reflector systems, such as the Cassegrain and Gregorian, are widely used in radio astronomy [2].
- Configuring the outrigger panel system by designing each alternating panel to null at different frequencies for broadband interference mitigation.
- Developing an algorithm to create a null at different frequencies while constraining the main lobe directivity.

- Deriving a closed form expression for the minimum rim width for the conformal ERS implementation when there are gaps. To determine this expression, a closed form expression for the projected area of the ERS must be found. With this expression, the procedure in Section 4.5 could be adjusted to determine the minimum width of the ERS for nulling when there are gaps.
- Performing a full-wave analysis on the outrigger panel configurations to validate the results of this thesis.
- Including diffraction from the edges of the outrigger panels to more accurately assess the performance of Cases A-D.

Appendix A

Outrigger Panel Geometry

This section derives the length of an outrigger panel, which is addressed in Section 5.1. This length is used to design the outrigger panels that circumscribe the rim of the non-reconfigurable portion of the reflector. First, we will solve for the side length of an equilateral triangle that circumscribes a circle with the same diameter as the non-reconfigurable portion of the circular edge of the reflector. Then, we will extend the result to a p-sided polygon, where p refers to the number of outrigger panels in Chapter 5.

See Figure A.1 for a diagram of an equilateral triangle with side length l that circumscribes a circle of radius r. The interior angle of each of the vertices, γ, is equal to $\pi/3$ rad. Since the triangle is equilateral, each intersection of the circle and the triangle must occur at a midpoint of each side of the triangle. Therefore, the distance from the center of the circle to each midpoint is r. From Figure A.1, we can draw two congruent triangles, with the bases of each triangle having length l_{base}. If the midpoint bisects each side of the triangle, then $l_{base} = l/2$. Since each triangle shares a hypotenuse, both triangles are congruent via the side-side-side theorem. Therefore,

$$l_{base} = \frac{r}{\tan(\gamma/2)} \tag{A.1}$$

Finally,

$$l = 2\ l_{base} = \frac{2r}{\tan(\gamma/2)} \tag{A.2}$$

We now extend this result to a p sided equilateral polygon. First, note

$$\gamma(p) = \frac{\pi(p-2)}{p}$$

Thus,

$$l = 2r\cot\left(\frac{\pi(p-2)}{2p}\right) \tag{A.3}$$

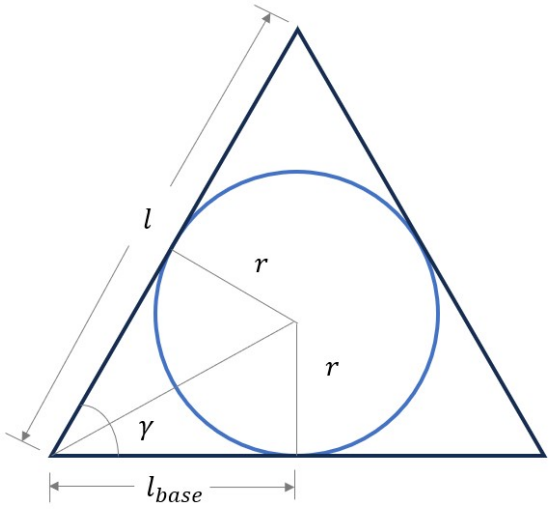

Figure A.1: Triangle circumscribing a circle of radius r.

Appendix B

Outrigger Panel Orientation

In this subsection, we derive the tangent angle of the rim of an axisymmetric paraboloidal reflector with respect to the axis of symmetry of the reflector, ψ, as shown in Figure B.1. This angle is necessary for orienting the outrigger panels, as described in Section 5.1.

Recall that the equation defining the paraboloid with vertex at the origin is as follows:

$$\rho^2 = 4fz \tag{B.1}$$

where ρ is the perpendicular distance from the z-axis and f is the focal length. Since we are interested in the tangent angle at the edge of the reflector, we can restrict our attention to a parabola in the xz-plane:

$$x^2 = 4fz \tag{B.2}$$

We can further restrict our attention to the case in which x is positive:

$$x = 2\sqrt{fz} \tag{B.3}$$

Taking the derivative of both sides with respect to z yields:

$$\frac{dx}{dz} = \sqrt{\frac{f}{z}} \tag{B.4}$$

At the rim, $x = D/2$, where D is the diameter of the non-reconfigurable portion of the reflector. Thus, $z = D^2/16f$ at this location. Therefore, the derivative at the rim is:

$$\frac{dx}{dz} = \frac{4f}{D} \tag{B.5}$$

Note that taking the arc-tangent of the derivative yields the angle with respect to the axis of symmetry of the reflector:

$$\psi = \arctan\frac{4f}{D} \tag{B.6}$$

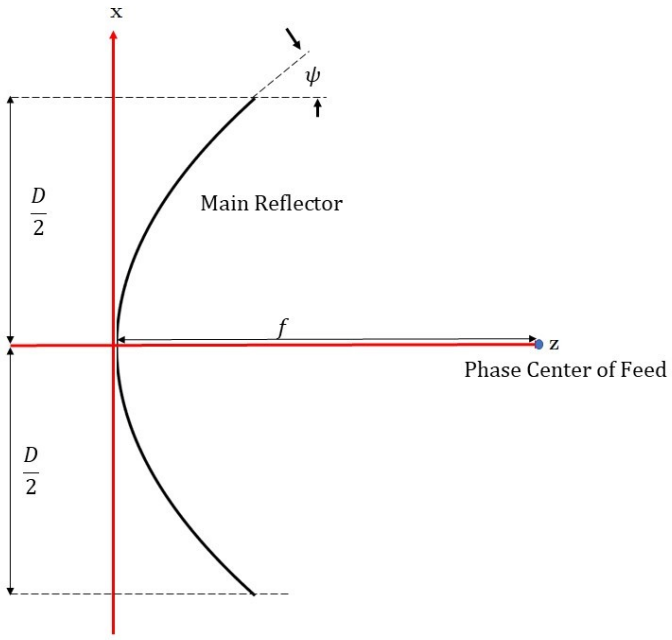

Figure B.1: Reflector geometry showing ψ.

Thus, the value of ψ computed by Equation B.6 is the orientation of the outrigger panels.

References

[1] B.F. Burke, F. Graham-Smith and P.N. Wilkinson, *An Introduction to Radio Astronomy*, 4th ed., Cambridge University Press, 2019.

[2] S.W. Ellingson, "Antennas in radio telescope systems," *Handbook of Antenna Technologies*, ed. by Zhi Ning Chen; Singapore: Springer Singapore, pp. 1–21, 2015.

[3] "20m," Green Bank Observatory, https://greenbankobservatory.org/about/telescopes/20m/ (accessed Jul 12, 2024).

[4] S. Joardar and J. R. Claycomb, *Radio Astronomy*, Dulles, VA, USA: Mercury Learning & Information, 2015.

[5] United Nations Office of Outer Space Affairs and the International Astronomical Union, "Dark and quiet skies for science and society: Report and recommendations," 2021. doi:10.5281/zenodo.5898785

[6] T.S. Bird, *Fundamentals of Aperture Antennas and Arrays: From Theory to Design, Fabrication and Testing,* Hoboken, NJ, USA: Wiley, 2016.

[7] S.W. Ellingson and R. Sengupta, "Sidelobe modification for reflector antennas by electronically reconfigurable rim scattering," *IEEE Antennas and Wireless Propagation Letters*, vol. 20, no. 6, pp. 1083–1087, Jun 2021. doi:10.1109/lawp.2021.3072536

[8] J Budhu, S.V. Hum, S.W. Ellingson, and R.M. Buehrer, "Loading rims of radio telescopes with reconfigurable reflectarrays for adaptive null-steering," *2024 United States National Committee of URSI National Radio Science Meeting*, Jan 2024. doi:10.23919/usnc-ursinrsm60317.2024.10464936.

[9] S.V. Hum, S.W. Ellingson, and R.M. Buehrer, "Reflectarray concept for interference mitigation in radio astronomy," *2023 IEEE International Symposium on Antennas and Propagation and USNC-URSI Radio Science Meeting*, Jul 2023. doi:10.1109/usnc-ursi52151.2023.10237818.

[10] R.M. Buehrer and S.W. Ellingson, "Weight selection for pattern control of paraboloidal reflector antennas with reconfigurable rim scattering," *2023 IEEE Aerospace Conference*, Mar 2023. doi:10.1109/aero55745.2023.10115669.

[11] W. Howard, R.M. Buehrer & S.W. Ellingson, "Open and Closed-Loop Weight Selection for Pattern Control of Paraboloidal Reflector Antennas with Reconfigurable Rim Scattering". Preprint: arXiv:2308.16339 [eess.SP](27 Feb 2024).

[12] J. Budhu, S.V. Hum, S.W. Ellingson, and R.M. Buehrer, "Design of rim-located reconfigurable reflectarrays for interference mitigation in reflector antennas," *IEEE Transactions on Antennas and Propagation*, vol. 72, no. 4, pp. 3736–3741, Apr. 2024. doi:10.1109/tap.2024.3352250.

[13] W. Stutzman and G. Thiele, *Antenna Theory and Design*, Wiley, 3rd ed. Hoboken, New Jersey, USA: Wiley, 2013.

[14] A.C Ludwig, "The definition of cross polarization," *IEEE Transactions on Antennas and Propagation*, vol. 21, no. 1, pp. 116–119, Jan 1973. doi:10.1109/tap.1973.1140406.

[15] R. Sengupta, "Adaptive pattern modeling for large reflector antennas", M.S. thesis, Virginia Tech, 2022.

[16] J. Stewart, "Calculating Limits Using the Limit Laws", *Calculus Early Transcendentals*, Cengage, 8th ed. Boston, MA, USA. Jan 2016